

# Evaporative silicification in floating microbial mats: patterns of oxygen production and preservation potential in silica-undersaturated streams, El Tatio, Chile

Dylan T. Wilmeth<sup>1,2</sup>  | Kimberly D. Myers<sup>1</sup> | Stefan V. Lalonde<sup>2</sup> | Kaarel Mänd<sup>3,4</sup> | Kurt O. Konhauser<sup>4</sup> | Prisca Grandin<sup>2</sup> | Mark A. van Zuilen<sup>1</sup>

<sup>1</sup>Université de Paris, Institut de Physique du Globe de Paris, CNRS, Paris, France

<sup>2</sup>CNRS-UMR6538, European Institute for Marine Studies, Plouzané, France

<sup>3</sup>Department of Geology, University of Tartu, Tartu, Estonia

<sup>4</sup>Department of Earth and Atmospheric Sciences, University of Alberta, Edmonton, Alberta, Canada

[Correction added on 02 November 2021, after first online publication: Affiliation 1 has been corrected in this version of the article.]

## Correspondence

Dylan T. Wilmeth, Institut de Physique du Globe de Paris, CNRS-UMR7514, Paris, France.

Email: dylan.wilmeth@univ-brest.fr

## Funding information

European Research Council

## Abstract

Microbial mats floating within multiple hydrothermally sourced streams in El Tatio, Chile, frequently exhibit brittle siliceous crusts (~1 mm thick) above the air–water interface. The partially silicified mats contain a diverse assemblage of microbial clades and metabolisms, including cyanobacteria performing oxygenic photosynthesis. Surficial crusts are composed of several amorphous silica layers containing well-preserved filaments (most likely cyanobacteria) and other cellular textures overlying EPS-rich unsilicified mats. Environmental logs, silica crust distribution, and microbial preservation patterns provide evidence for crust formation via repeated cycles of evaporation and silica precipitation. Within the mats, in situ microelectrode profiling reveals that daytime oxygen concentrations and pH values are diminished beneath silica crusts compared with adjacent unencrusted communities, indicating localized inhibition of oxygenic photosynthesis due to light attenuation. As a result, aqueous conditions under encrusted mats have a higher saturation state with regard to amorphous silica compared with adjacent, more active mats where high pH increases silica solubility, likely forming a modest feedback loop between diminished photosynthesis and crust precipitation. However, no fully lithified sinters are associated with floating encrusted mats in El Tatio streams, as both subaqueous and subaerial silica precipitation are limited by undersaturated, low-SiO<sub>2</sub> (<150 ppm) stream waters. By contrast, well-cemented sinters can form by evaporation in silica-undersaturated solutions above 200 ppm SiO<sub>2</sub>. Floating mats in El Tatio therefore represent a specific sinter preservation window, where evaporation in silica-undersaturated microbial mats produces crusts, which preserve cells and affect mat chemistry, but low-silica concentrations prevent the formation of lasting sinter deposits. Patterns of silica precipitation in El Tatio microbial communities show that the preservation potential of silicifying mats in the rock record is strongly dependent on aqueous silica concentrations.

## KEYWORDS

biomineralization, El Tatio, microbial mat, silicification, sinter

This is an open access article under the terms of the Creative Commons Attribution-NonCommercial-NoDerivs License, which permits use and distribution in any medium, provided the original work is properly cited, the use is non-commercial and no modifications or adaptations are made.

© 2021 The Authors. *Geobiology* published by John Wiley & Sons Ltd.

## 1 | INTRODUCTION

Microbial mats are generally mixed communities of micro-organisms that form layered macroscopic textures up to several cm thick. In certain environments, extensive mineral precipitation within microbial mats leads to the formation of microbialites: lithified structures that preserve mat textures on macro- and microscopic scales. Modern environments contain abundant examples of microbial mats and microbialites, particularly in terrestrial hydrothermal settings, such as hot springs, where discharged fluids contain high concentrations of silica, carbonates, iron oxides, and other minerals (Fouke et al., 2000; Fouke, 2011; Jones & Renaut, 1996; Jones et al., 2004; Konhauser & Ferris, 1996; Parenteau & Cady, 2010; Schultze-Lam et al., 1995; Walter, 1976; Wilmeth et al., 2018).

Hydrothermal mats are commonly preserved in siliceous sinters as amorphous silica (opal-A) precipitates from supersaturated solutions. At temperatures of 25°C and pH values below 8, amorphous silica solubility is ~110 ppm SiO<sub>2</sub>, increasing with temperature to 175 ppm at 50°C and 380 ppm at 100°C (Gunnarsson and Arnórsson 2000). Silica solubility also increases with pH in solutions higher than pH 8; at 50°C, silica solubility increases from 180 ppm SiO<sub>2</sub> (pH 8) to 260 ppm (pH 9) to 1050 ppm (pH 10) (Alexander et al., 1954). Sinter precipitation is therefore governed by multiple environmental factors, forming a variety of textures, which preserve aspects of local biology, geochemistry, and the physical environment (Cady & Farmer, 1996; Campbell et al., 2015; Jones et al., 1997, 1998, 2005; Gong et al. 2020; in review; Handley et al., 2005; Konhauser & Ferris, 1996; Konhauser et al., 2001; Konhauser et al., 2003; Orange et al., 2013; Schultze-Lam et al., 1995; Walter, 1976). Siliceous sinters occur throughout the rock record up to 3.5 billion years ago (Ga) and include the earliest evidence for life in non-marine environments (Djokic et al., 2017). Sinter deposits ~3.8 Ga are also preserved on Mars, presenting targets for future investigations of sedimentology and potential astrobiological signatures (Ruff et al., 2020; Ruff & Farmer, 2016). Therefore, the continuing investigation of microbial silicification is highly relevant for understanding biosignature preservation in modern and ancient sedimentary deposits both on Earth and potentially elsewhere in our solar system.

Microbial silicification is generally considered to be a passive process occurring in supersaturated solutions, as opposed to “biologically induced” precipitation resulting from metabolic biochemistry (e.g., oxygenic photosynthesis, respiration) (Weiner & Dove, 2003; Dupraz et al., 2009; Konhauser et al., 2004). Negatively charged silica molecules bind to positively charged substrates in mats including organic functional groups such as amines, or surficial cations, which are already bonded to more negative organic substrates (Benning et al., 2004; Lalonde et al., 2005; Leo & Barghoorn, 1976; Moore et al., 2021; Phoenix et al., 2002, 2003; Yee et al., 2003). While microbes do not appear to actively control the polymerization of silica via metabolic pathways, individual organisms can physically influence silicification patterns by producing higher concentrations of positively charged organic compounds away from cell interiors. Microbes can shift silica nucleation and precipitation to thick exterior sheaths immediately adjacent to cell walls (Benning et al., 2004),

or to surfaces within surrounding extrapolymeric substances (EPS) (Lalonde et al., 2005).

As long as silica precipitation does not occur within individual cells, microbes can survive and even benefit from pervasive silicification (Phoenix & Konhauser, 2008). One of the most notable advantage of silicification to micro-organisms is protection from damaging UV radiation, especially in subaerially exposed, high elevation habitats (Cnossen et al., 2007; Havig & Hamilton, 2019; Phoenix et al., 2006). Opal-A can serve as a selective “sunscreen” for cells, with 2- $\mu$ m-thick coatings blocking up to 80% of UV radiation, while removing only 20% of photosynthetically active radiation (PAR; Phoenix et al., 2006). At depths greater than 4 mm, opal-A crusts absorb virtually all UV radiation while still providing enough PAR (3% incident radiation) for cyanobacteria to survive in most environments (Phoenix et al., 2006). Surface environments on early Earth were likely subjected to high UV exposure, and silica crusts potentially formed sanctuaries for ancient microbes to avoid extensive cellular damage (Phoenix et al., 2001).

While localized silicification can be beneficial to microbes, the progressive transformation of a microbial mat into a microbialite is ultimately detrimental to portions of the affected community. Partially silicified living mats provide unique opportunities to study such transitions in the field and also serve as useful analogues for ancient conditions of microbialite preservation. The larger-scale effects of silicification on microbial communities can be assessed by comparing chemical gradients between different mat regions experiencing various stages of silicification. Mat chemistry is frequently measured by vertical microprofiles through successive layers (Epping & Kuhl, 2000; Jorgensen et al., 1983; Revsbech et al., 1983; Wieland and Kuhl 2000); however, no studies have yet profiled mats actively undergoing silicification.

Here, we describe living microbial mats experiencing silicification in El Tatio, Chile, including the first chemical profiles from a silicifying mat. This study has three goals: (1) to determine the physical and/or biological parameters influencing silica precipitation in the El Tatio mats, (2) to determine the effects of progressive silicification on mat communities, and (3) to determine the preservation potential of observed silicifying mats in the rock record. Microprofiles of O<sub>2</sub> and pH were obtained within mats at different stages of silicification, forming two-dimensional transects of subsurface chemistry. Shifts in local aqueous and atmospheric parameters known to influence the physical process of silicification (e.g., water temperature, relative humidity) were also monitored over several days. The composition, structure, and function of microbial communities were examined using DNA analyses and scanning electron microscopy (SEM). The combined datasets provide insight into the interactions between local environmental parameters, silica precipitation, and microbial metabolisms, as well as the preservation potential of silicifying mats.

## 2 | LOCATION

The El Tatio geothermal field is located in the Andes Mountains of northern Chile, 80 km north of San Pedro de Atacama (Figure 1a).

El Tatio contains the world's highest geyser field (~4300 m), and the largest geyser field in the Southern Hemisphere (~30 km<sup>2</sup>) (Glennon & Pfaff, 2003; Jones & Renaut, 1997; Munoz-Saez et al., 2018; Tassi et al., 2005; Trujillo 1969; Zeil, 1959). The extreme altitude of El Tatio produces a unique environment relative to other hydrothermal

localities. At 4300 m elevation, atmospheric pressure is 0.58 atm, oxygen partial pressure is 0.12 atm, and the boiling point of water is 86°C. Daily temperatures vary between -5 and 25°C during spring (Munoz-Saez et al., 2015) and drop to -30°C in winter (Fernandez-Turiel et al., 2005), resulting in frequent freeze-thaw cycles (Nicolau et al., 2014). Wind speeds also follow daily cycles, increasing to 7 km/h in the early afternoon (Slagter et al., 2019). El Tatio is located in the arid Chilean Altiplano, receiving a mean annual precipitation of 44 mm/year (DGA, 2017). Ultraviolet radiation levels are also elevated, with maximum UV-A and UV-B levels at 33 and 6 W/m<sup>2</sup>, respectively (Phoenix et al., 2006). The high ultraviolet radiation and lower atmospheric pressure at El Tatio provide a potential analogue to conditions modeled on early Earth and Mars (Cockell, 2000; Ruff & Farmer, 2016; Som et al., 2012, 2016).

El Tatio is divided into three basins: Upper, Middle, and Lower, with most hydrothermal activity concentrated in the Upper Basin (Figure 1b). Microbial mats were analyzed in two locations. Mat microprofiles, SiO<sub>2</sub> concentrations, long-term environmental logs, and mat samples for DNA and SEM analyses were collected from Vicuña Stream (Figures 1b, 2a–c), a perennial stream fed by geothermal runoff and shallow steam-heated vents within the Upper Basin (22.330 S, 68.008 W). Waters upstream of the mat locality are cool (<25°C), shallow (<5 cm depth), and form a braided channel between 2 and 3 meters wide flowing south, filled with eukaryotic plants and algae. At the uppermost portion of the mats presented in this study, Vicuña Stream's flow drops over a 15-cm-high ledge and funnels into a 52°C pool (50 cm wide and 20 cm deep), followed by a single channel of equal width flowing south (Figure 2a). Benthic biological communities immediately change upon contact with the warmer pool water, switching from brown grasses to microbial mats with various shades of green and orange (Figure 2b). Mats continue to dominate benthic surfaces for more than six meters downstream (Figure 2a), although this study primarily focused on locations in the first 2 m downstream of the hydrothermal pool. Physical textures of microbial mats are provided in greater detail in Section 4.3.

Partially silicified mat samples were also collected for DNA and SEM analyses from a similar location along a perennial geothermal runoff known as the Middle Basin Springs (Figure 1b, 22.343 S, 68.0113 W), described previously in Plenge et al. (2017). As with Vicuña Stream, silica-encrusted mats in Middle Basin Springs occur downstream from a secondary hydrothermal pool (67°C) within the channel (Figure 2d–f). The channel is between 1 and 2 m wide, with an average depth of 20 cm. Mats are present for more than 10 m downstream, although samples were only collected from silicifying mats 2 m downstream of the hydrothermal pool.

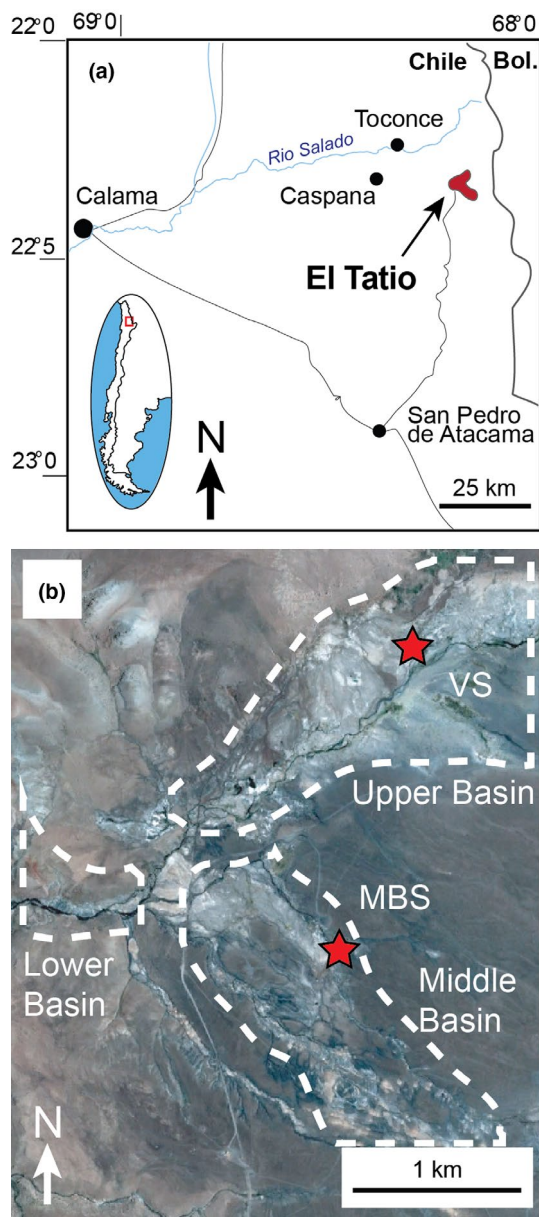


**FIGURE 1** Location maps. (a) Location of El Tatio within Chile. (b) Locations of Vicuña Stream (VS) and Middle Basin Springs (MBS) in the Upper and Middle Basins of El Tatio, respectively

**FIGURE 2** Sampling locations: a–c from Vicuña Stream and d–f from Middle Basin Springs. (a) Upstream view of Vicuña Stream, with floating olive unencrusted microbial mats lining stream margins and forming “islands” within the channel. The stream's source is shown in the upper-left corner. (b) Overhead view of Vicuña Stream source with orange, olive, and dark green mats. Olive encrusted mats contain more extensive white silica crusts on the east bank. Submerged benthic mats in the center of the pool occur 20–30 cm below floating mats. (c) Olive encrusted and unencrusted mats between dark green fringes and orange mats on the east bank of Vicuña Stream, 1–2 m downstream of source. Red star represents a quadruplicate microprofile location (see Figure 7), while yellow stars are microprofile transects (see Figure 8). (d) Downstream view of Middle Basin Springs (MBS). (e) Floating olive encrusted mats in MBS, with two cobbles rising above mat level. (f) Close-up of silicifying MBS mats. Pen is 15 cm for scale

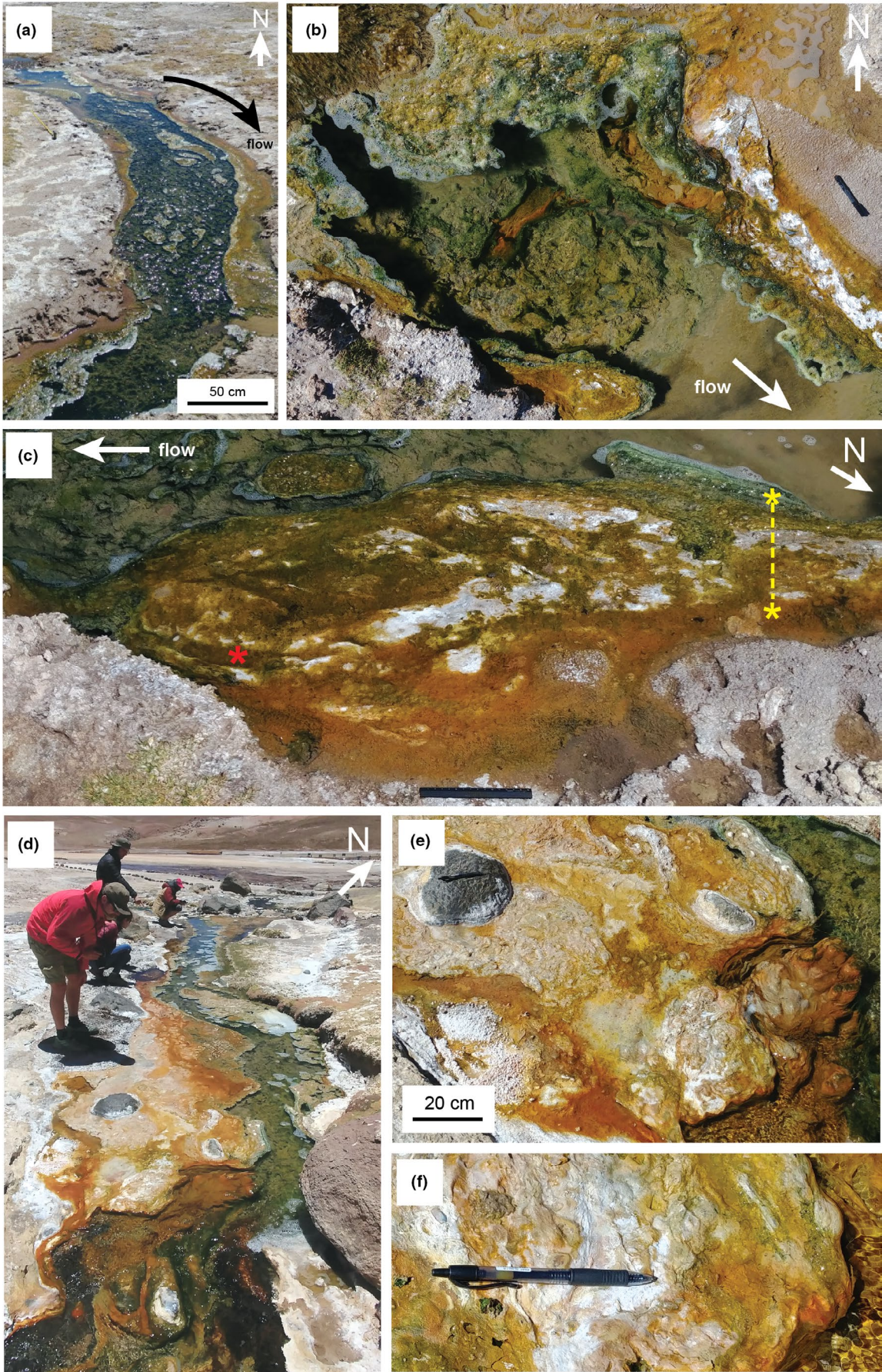


TABLE 1 Sample locations and descriptions from Vicuna Stream and Middle Basin Springs

Location	Distance from pool margin	Description	Surficial T (°C)	Floor T (°C)	SiO <sub>2</sub> (ppm)	DNA	Microprofiles
Vicuna Stream	20 cm	Surface mat, olive (north pool margin)	48.9	52.0	-		
Vicuna Stream	70 cm	Center of pool (mats on floor)	52.6	45.3	140 ± 7		
Vicuna Stream	130 cm	Center of stream, no mats	48.2	32.6	-		
Vicuna Stream	130 cm	Surface mat, orange tufts (east bank)	35.4	40.8	-	VS-1	y
Vicuna Stream	130 cm	Surface mat, olive + silica crust (east bank)	39.3	43.1	131 ± 7	VS-2, 3	y
Vicuna Stream	130 cm	Surface mat, dark green margin (east bank)	45.1	46.5	-	VS-4	y
Vicuna Stream	440 cm	Surface mat, olive + silica crust- central island	41.0	47.6	114 ± 6		
Vicuna Stream	630 cm	Surface mat, olive (east bank)	29.4	42.0	102 ± 5		
Middle Basin Springs	220 cm	Surface mat, olive + silica crust (west bank)	39.3	55.6	-	MBS-2	
Middle Basin Springs	200 cm	Surface mat, olive + silica crust (west bank)	61.1	66.0	-	MBS-4	

Note: Temperatures were taken within one centimeter of the air-water and sediment interfaces for surficial and floor measurements, respectively. Silica concentrations and DNA samples were sampled within one centimeter of the air-water interface.

### 3 | METHODS

#### 3.1 | Microprofiles

Microprofiles of O<sub>2</sub> and pH were measured in Vicuna Stream mats using 50-μm-wide glass microsensors (OX-50 and PH-50, Unisense A/S). Both microsensors were secured three cm apart on a double-headed micro-manipulator (MM-33-2, Unisense A/S) attached to an in situ field stand, for simultaneous measurements of O<sub>2</sub> and pH within mats. Therefore, while coupled O<sub>2</sub> and pH profiles presented in data and figures were not taken from the same mat coordinates, profiles were measured three cm apart at the same time, from mat surfaces with similar visual and physical properties (see Section 4.6).

The in situ stand was secured on the east bank of Vicuna Stream, while both microsensors were lowered into mats at 1 mm intervals by manually adjusting the micro-manipulator. For mat surfaces with brittle silica crusts, a metal needle was used to puncture through crusts immediately prior to microprofiling, to prevent the microsensor from breaking. Punctures were limited to the upper 1–2 mm of mat surfaces, to prevent mixing of surface and deeper waters.

O<sub>2</sub> and pH measurements were recorded at each depth using the program SensorTrace Suite (Unisense A/S), after equilibration times of ~3 s. SensorTrace was also used to calibrate O<sub>2</sub> and pH meters prior to field measurements. O<sub>2</sub> microsensors were calibrated using aerated water (atmospheric O<sub>2</sub>) and ~2 g sodium ascorbate in 100 ml of 0.1 M NaOH (0% O<sub>2</sub>). pH microsensors were calibrated using buffers at pH 4, 7, and 10. Microsensor data were converted from mV to milli-molar concentrations of oxygen [O<sub>2</sub>] using the following equation, where [a] = the solubility concentration of O<sub>2</sub> at the water

temperature and air pressure of field conditions (mM), S = signal measured from a microbial community (mV), S<sub>0</sub> = signal calibrated within the 0% O<sub>2</sub> solution, and S<sub>sat</sub> = signal calibrated within aerated stream waters (mV):

$$[O_2] = [a] * ((S - S_0) / (S_{sat} - S_0))$$

Measurements of photosynthetic rates within mats using light-dark techniques were not implemented at Vicuna Stream due to safety concerns. Multiple microelectrode profiles were visualized in 2D transects via cubic surface interpolation using the griddata and contourf functions in the software package Matlab.

#### 3.2 | Environmental loggers and temperature profile

Weather data were collected at Vicuna Stream from April 26 to April 28 with a portable weather meter mounted 37 cm above ground level, adjacent to silicifying mats (Kestrel 5500, Kestrel Instruments). Data points were collected at 1-minute intervals including wind speed, air temperature, and humidity. Water temperature and ambient light level were recorded over the same period of time within surficial mats (1.3 m downstream of the pool's north shore) with data loggers (HOBO MX2202 and MX2203, Onset Computer Co. MX2202: temperature accuracy ± 0.5°C, range -20 to 70°C in air and -20 to 50°C in water; light level accuracy ± 10% for direct sunlight, range 0 to 167,731 lux. MX2203: temperature accuracy ± 0.25°C from -20° to 0°C and ±0.2°C from 0 to 70°C). Water temperatures were logged with the sensor fully submerged. Full datasets for all logged parameters are available in Table S1. Water temperature data were also

collected using a Traceable thermometer (range:  $-50$  to  $300^{\circ}\text{C}$ , accuracy  $\pm 1^{\circ}\text{C}$ ) as a stream profile at 15:00 when stream waters were warmest (Table 1, Figure 4). A visual time-lapse of Vicuna Stream mats over six hours (10:00 to 16:00 hours) was recorded using a GoPro camera (Video S1).

### 3.3 | $\text{SiO}_2$ concentrations

Water samples ( $n = 4$ ) were collected from four locations in Vicuna Stream (Table 1), one within the source pool, and three adjacent to mats further downstream (0.7, 1.3, 4.0, and 6.0 m from the pool's north edge). Samples were collected in syringes fitted with  $0.2\text{-}\mu\text{m}$  filters to minimize contamination from extraneous silica sources such as diatoms. Silica concentrations were determined at the Institut de Physique du Globe de Paris (IPGP, Paris, France) using a HACH DR9000 multiparameter portable colorimeter. To account for potential changes in sample temperature and pH during transportation, water samples were heated to appropriate temperatures for one hour before analysis. Laboratory pH values for water samples matched field values recorded in Vicuna Stream ( $\text{pH} = 6.8$ ). Detailed methods for silica colorimetry are publicly available in the HACH silicomolybdate HR protocol 8185.  $\text{SiO}_2$  concentrations reported have error ranges of  $\pm 5\%$ , based on measurements of 50, 100, and 150 ppm  $\text{SiO}_2$  standards. Amorphous silica solubility was calculated for solutions at various temperatures and pH values using the free geochemistry software package vMINTeq (<https://vminteq.lwr.kth.se>), which uses literature sources within the publicly accessible NIST Critically Selected Stability Constants of Metal Complexes Database (Smith et al., 22004).

### 3.4 | Scanning electron microscopy

Mat samples were taken for scanning electron microscopy (SEM) from Vicuna Stream and Middle Basin Springs. Unfortunately, samples from Vicuna Stream were contaminated with mold upon return to the laboratory, while Middle Basin samples were still well-preserved. Therefore, SEM images do not represent the same locality as the microprofiles and environmental data collected from Vicuna Stream. However, the physical and visual properties of both biological communities, overlying silica crusts, and surrounding physical environments support similar patterns of silicification between the two locations (Figures 2, 3, Table 1).

SEM was performed on planar surfaces of five Middle Basin Springs mat samples fractured into 3- to 5-mm pieces. Samples were prepared in 2.5% glutaraldehyde in the field and stored at  $4^{\circ}\text{C}$  prior to analysis. Before imaging, samples were rinsed with deionized water and air-dried before being placed directly on aluminum stages with carbon glue and sputter-coated with gold. SEM images were obtained at the IPGP PARI analytical platform with a Zeiss EVO MA-10, at 15 kV and 12-mm working distance on SE mode.

Energy dispersive X-ray spectroscopy was performed on the same Zeiss SEM to examine the elemental composition of crusts on top of microbial mats.

### 3.5 | DNA sampling and analysis

Microbial mat samples were collected in bulk using sterile technique from both Vicuna Stream and Middle Basin Springs. In Vicuna Stream, samples were taken adjacent to three  $\text{O}_2$  and pH microprofiling locations  $\sim 1.3$  m downstream of the confluence of hydrothermal vents and a geothermal runoff stream, along a transect extending from the stream bank to the advancing front of the actively growing mat, perpendicular to the stream bank and the direction of flow (Table 1). Samples were collected corresponding to different mat colors, silicification styles, and mat textures: (1) orange, tufted mat (VS-1), (2) olive unencrusted mat (VS-2A, 2B), (3) olive silica-encrusted mat (VS-3) and (4) dark green mat margins (VS-4) (see Section 4.3 for additional detail), in order to investigate the community composition and structure of micro-organisms alongside in situ geochemical and physical parameters. In Middle Basin Springs, samples were collected from two locations: (1) olive, silica-encrusted surfaces in the center of mats (MBS-2), and (2) olive, silica-encrusted surfaces along warmer mat margins (MBS 4) (Table 1). In both locations, samples were immediately placed in sterile bags and stored between  $0$  and  $4^{\circ}\text{C}$  in thermal insulating bags until reaching the laboratory. Within 1 week of sampling, samples were frozen at  $-20^{\circ}\text{C}$  to preserve DNA.

Genomic DNA was extracted using a Qiagen™ DNeasy® PowerLyzer® PowerSoil® kit (Qiagen Sciences, Germantown MD USA) following manufacturer protocols. The V4-5 region of the 16S rRNA gene (515f-926r) (Walters et al., 2016) was sequenced to a depth of  $\sim 100\text{k}$  reads/sample on an Illumina MiSeq (Illumina Inc., San Diego CA, USA) platform (MrDNA Labs, Shallowater, TX, USA) using bacterial tag-encoded FLX amplicon (bTEFAP®) sequencing technology (Dowd et al., 2008). Following standard quality control removal steps (Caporaso et al., 2010), filtered, quality-, and chimera-checked 16S amplicon libraries containing an average of 70k reads/sample were aligned to cultured, database-accessioned environmental clones using the most recent Greengenes (v. 13.8) alignment database (DeSantis et al., 2006).

Generic and species-level taxonomic assignments were made at the 97% and 99% cutoff levels, respectively (Table S2). Resulting quality- and chimera-checked 16S amplicon libraries contained an average of 70k reads/sample. Abundant ( $>0.1\%$  relative abundance) organisms were researched and categorized into primary categories of (1) metabolic growth physiology and (2) aerotolerance in order to assess changes in community function alongside the taxonomic structure (% relative abundance) of the classified OTUs identified in each sample. Functional assignments were made based on physiological studies of cultured representatives of OTU assignments at the generic level.

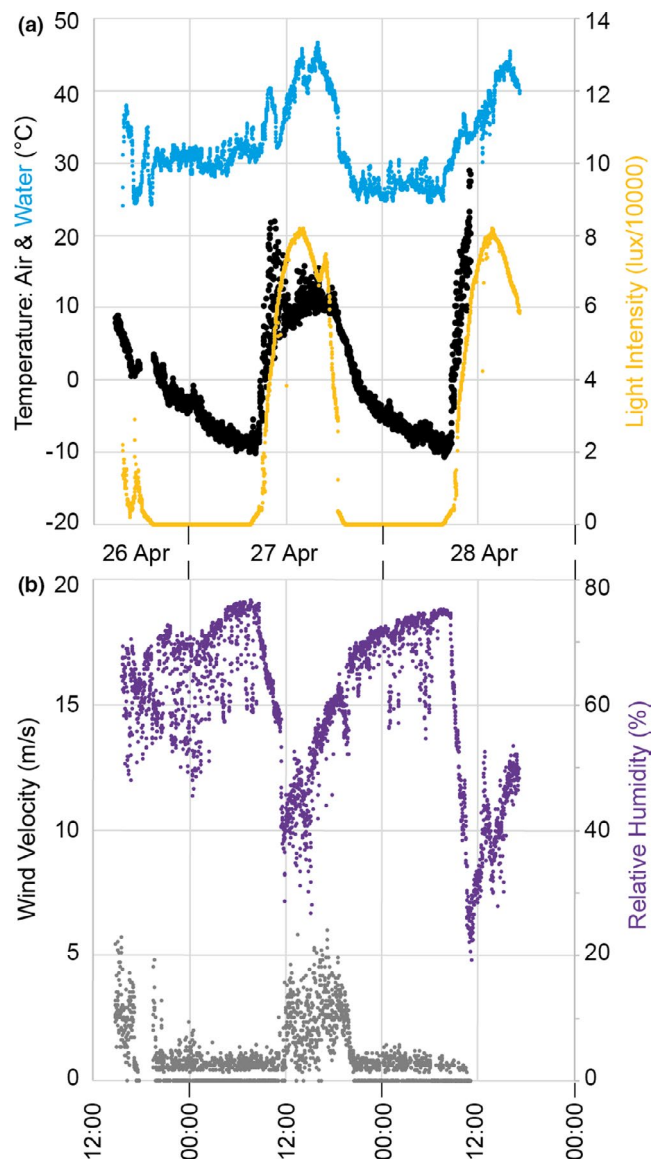


**FIGURE 3** Environmental logs from Vicuna Stream. (a) Light intensity (lux, yellow) with air and water temperatures (°C, blue and black). (b) Relative humidity (% purple) and wind velocity (m/s, gray)

## 4 | RESULTS

### 4.1 | Environmental conditions

Many environmental parameters fluctuate on diel cycles at Vicuna Stream (Figure 3). Sunrise and sunset occurred at 07:45 and 19:15, respectively, with higher light intensities between 09:00 and 18:00 hours. After 09:00 hours, air temperatures quickly rose from  $-10$  to over  $20^{\circ}\text{C}$  within 2 h, stabilizing between 9 and  $15^{\circ}\text{C}$  until 18:00 (Figure 3). As morning air temperatures rose, humidity sharply decreased from 78% to 30% at noon, then increased with windier afternoon conditions on the basin floor (5 m/s). Even after east-blowing winds diminished around sunset, humidity slowly continued to increase at night (Figure 3).

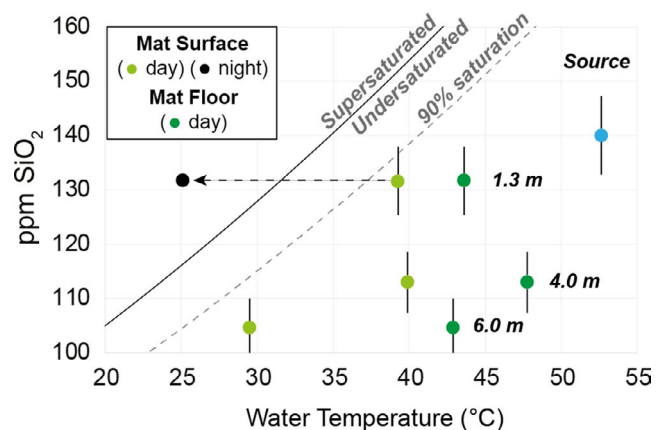


**FIGURE 4** Aqueous  $\text{SiO}_2$  solubility (ppm) vs. temperature ( $^{\circ}\text{C}$ ) in Vicuna Stream (pH = 6.8). Daytime temperatures (light and dark green) represent conditions during aqueous sample collection. Nighttime water temperatures in mats 1.3 m downstream (black) represent the minimum value recorded during environmental logging (see Figure 3)

In mats 1.3 meters downstream from the main hydrothermal pool, water temperatures varied between 25 and  $32^{\circ}\text{C}$  at night, gradually increasing during daylight hours to  $\sim 45^{\circ}\text{C}$  and dropping during sunset (Figure 3). A profile of stream temperatures was taken at 15:00, around peak values for Vicuna Stream (Table 1, Figure 4). The profile corroborates the in situ logger data at 1.3 m, showing a gradual cooling trend downstream over 6 m ( $52$ – $29^{\circ}\text{C}$ ). Notably, both surficial and basal mats 4 m downstream from the hydrothermal pool are warmer than mats at 1.3 m, presumably due to minor hydrothermal influxes along stream flow. Cooling trends were also observed in surficial mats and waters with increasing proximity to the stream bank (Table 1). Vertical temperature profiles varied based on the presence or absence of microbial mats. Temperatures in mat-free waters at the center of the pool and stream (Table 1) decreased downward from surface to underlying sediments. Conversely, all mats (Table 1) were warmer at their bases than surfaces, in some cases by  $12^{\circ}\text{C}$  ( $29.4$  vs.  $42.0^{\circ}\text{C}$ ). Stream pH values varied between 6.6 and 7.0, with an average of 6.8.

### 4.2 | $\text{SiO}_2$ concentrations

$\text{SiO}_2$  concentrations are  $140 \pm 7$  ppm within the main hydrothermal pool in Vicuna Stream (Table 1, Figure 4). The main hydrothermal pool is silica-undersaturated at pH 6.8 and temperatures above  $40^{\circ}\text{C}$ , with calculated solubility concentrations of 175 ppm  $\text{SiO}_2$  in surficial waters ( $52.6^{\circ}\text{C}$ ) and 161 ppm  $\text{SiO}_2$  on the stream floor ( $45.3^{\circ}\text{C}$ ) (Figure 4).  $\text{SiO}_2$  concentrations decrease downstream, eventually reaching  $\sim 102 \pm 5$  ppm  $\text{SiO}_2$  in waters 6 m downstream. In warmer waters during daylight, all measured locations are silica-undersaturated at ambient stream pH values 6.8 (Figure 4). For example, silica concentrations in surficial mats 1.3 m and 4.8 m downstream (131 and 114 ppm  $\text{SiO}_2$ , respectively) are lower than

solubility concentrations of 146 ppm  $\text{SiO}_2$  in afternoon conditions (40°C and pH 6.8).

As stream temperatures decrease at nighttime, conditions become more favorable for silica supersaturation. While daytime stream temperatures were measured by hand at various locations (Table 1) and using a HOBO data logger 1.3 m downstream (Figure 3), nighttime temperatures for surficial mats in Vicuna Stream were only measured with the HOBO data logger. At 1.3 m downstream, nighttime temperatures decreased to 25°C (Figure 3). At this location, silica concentrations in mats (131 ppm  $\text{SiO}_2$ ) are higher than calculated solubility concentrations of 110 ppm  $\text{SiO}_2$  (40°C and pH 6.8), producing silica-supersaturated solutions (Figure 4). Nighttime temperatures were not measured in mats farther downstream (4 and 6 m), but silica concentrations at each location (114 and 102 ppm  $\text{SiO}_2$ , respectively) would be near or below saturation at 25°C (solubility = 110 ppm  $\text{SiO}_2$ ) (Figure 4).

### 4.3 | Surficial mat characteristics

Floating rafts of bubble-rich microbial mats line the edges of Vicuna Stream and Middle Basin Springs. Floating mats persist for several meters downstream of hydrothermal pools in both locations (~6 m for Vicuna Stream, ~10 m for Middle Basin Springs) (Figures 2, 5). Mats widen and narrow corresponding to stream width, extending up to 1 m into channel flow. Flat-topped islands of microbial mats also form in the middle of wider stream sections (Figures 1a, 2c, Figure S1), reaching the air–water interface. Rich benthic mats line the hydrothermal pool floors at 20 cm depth, but do not form floating structures, and are separate from mat islands further downstream (Figure 2b).

Floating microbial mats form four distinct textures: (1) orange tufted mats, (2) olive unencrusted mats, (3) olive encrusted mats, and (4) dark green mat margins. Texture zones typically correspond with proximity to stream banks; orange mats line the stream's sides, progressing outward into olive surfaces before terminating in dark green fringes extending into channel flow (Figure 5). Boundaries between surficial textures can be sharp or gradational.

Orange conical textures are submerged in calmer pools, resting on top of mats proximal to stream banks in Vicuna Stream (Figure 5a, b), as well as more distal mats in Middle Basin Springs (Figure 2d, e). Orange zones can be extensive within shallow embayments (Figure 2c) but are usually confined within 5 cm bands (Figure 5a). Orange mat textures are rarely subaerially exposed, and almost never have silica crusts.

Olive unencrusted mat textures are the most abundant surfaces in Vicuna Stream and Middle Basin Springs, forming bands up to 20 cm between orange and dark green zones (Figure 5). Beyond 2 m downstream, mats are almost wholly composed of olive unencrusted textures. Olive mats are relatively buoyant, resulting in more frequent exposure above the air–water interface than orange or dark green surfaces. Time-lapse footage over six hours reveals extensive growth of cm-scale bubbles over large areas of olive mats and adjacent orange mats (Video S1).

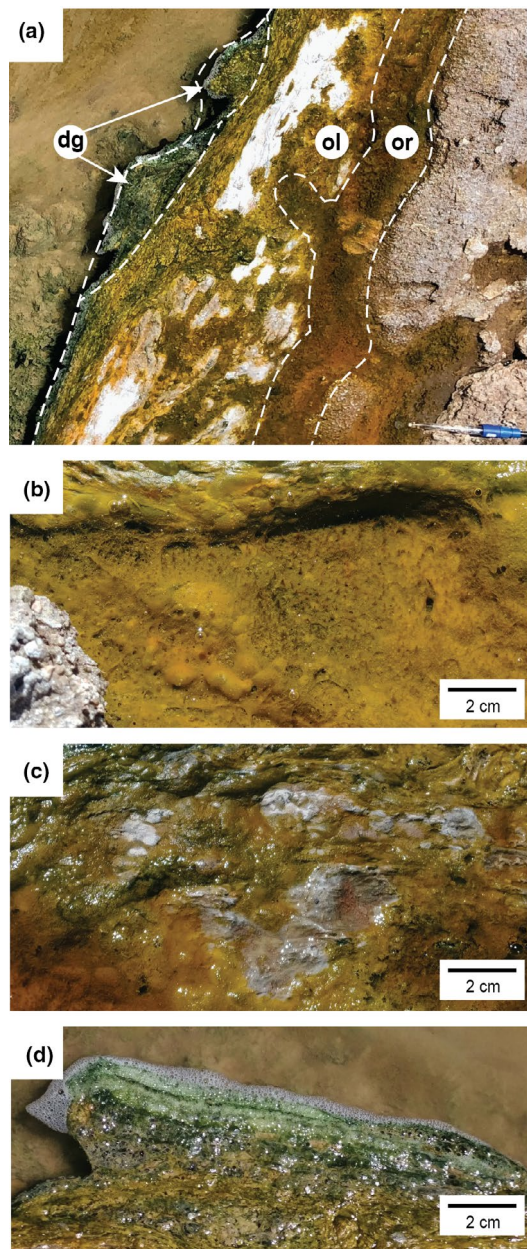


**FIGURE 5** Surficial characteristics of floating mats. (a) East bank of Vicuna Stream, 1 m downstream, showing orange mats (or) adjacent to stream margins, olive mats (ol) with varying amounts of subaerial silica crusts, and dark green mat fringes (dg). (b) Orange mats, highlighting cm-scale bubbles and mm-scale tufts. (c) Olive subaerial mats, highlighting gray-white silica crusts. (d) Dark green mat fringes, with abundant bubble textures and no silica crusts

Olive encrusted mat surfaces are the predominately silicifying zones in the streams (Figure 5). Silica crusts are up to 2 mm thick and typically occur above the air–water interface, although large portions of subaerial mats are not visibly silicified (Figures 2, 5). Silica crusts cover ~10-to-75% of olive mat surface areas, while orange and dark green mats have less than 10% silica coverage (Figure 5a). Silicified textures occur as far as 6 m downstream but decrease in areal coverage beyond 2 m distance. Encrusted mats are more abundant on the

east bank of Vicuna Stream, with small patches also occurring on the western bank (Figure 2b, c). Wet silica crusts are pale gray, becoming white and highly reflective upon drying (Figures 2, 5). Uppermost crusts are brittle and fragile, exhibiting slightly more ductile behavior over large areas due to the plasticity of underlying mats.

Dark green mats form thin fringes (three cm wide) along outer mat edges in Vicuna Stream (Figure 5a, d). Fringes are both subaqueous and subaerially exposed, but rarely contain silica crusts. Dark green fringes are most abundant within the first two meters of Vicuna Stream proximal to the hydrothermal vents (Figures 2a–c, 5) and are rarely observed in Middle Basin Springs (Figure 2d–f).

#### 4.4 | Mat community composition and function

Microbial mats in Vicuna Stream were sampled at four locations along the transect alongside pH and O<sub>2</sub> microprofiling locations corresponding to different surficial mat textures (Figures 2c, 5a). The aim was to target the microbial composition and metabolic function of (1) orange tufted mats, (2) olive mats without silica crusts, (3) encrusted olive mats, and (4) dark green mat margins growing rapidly outward over the flowing stream (Figure S1). Distinct differences in community composition are visible among the three mat types, and the relative proportions of various growth physiologies and aerotolerances shift across the mat types along the transect (Figure S1, Table S2). Percentages for taxa and growth physiologies represent relative abundance within mat samples.

An orange tufted mat was sampled in shallow, relatively cool (36.2°C) pools of water adjacent to the Vicuna Stream bank (Figure 5a, b, Table 1). This mat type is mainly composed of non-fermentative, aerobic heterotrophs (77.2%), a category dominated by the Phylum Planctomycetes including *Isosphaera pallida* (60.5%) (Figure S1, Table S2). Facultatively anaerobic heterotrophs are also prevalent in orange mats, dominated by members of the Phylum Bacteroidetes (*Cytophaga* sp., 5.2%) and various Proteobacteria (<1.0%). Aerobic, oxygenic photoautotrophs (Phylum Cyanobacteria) only comprise 3.0% of the total community, represented by filamentous *Leptolyngbya* sp. (1.2%) and unicellular *Cyanobacterium aponinum* (0.9%) and other rare species (<0.5%).

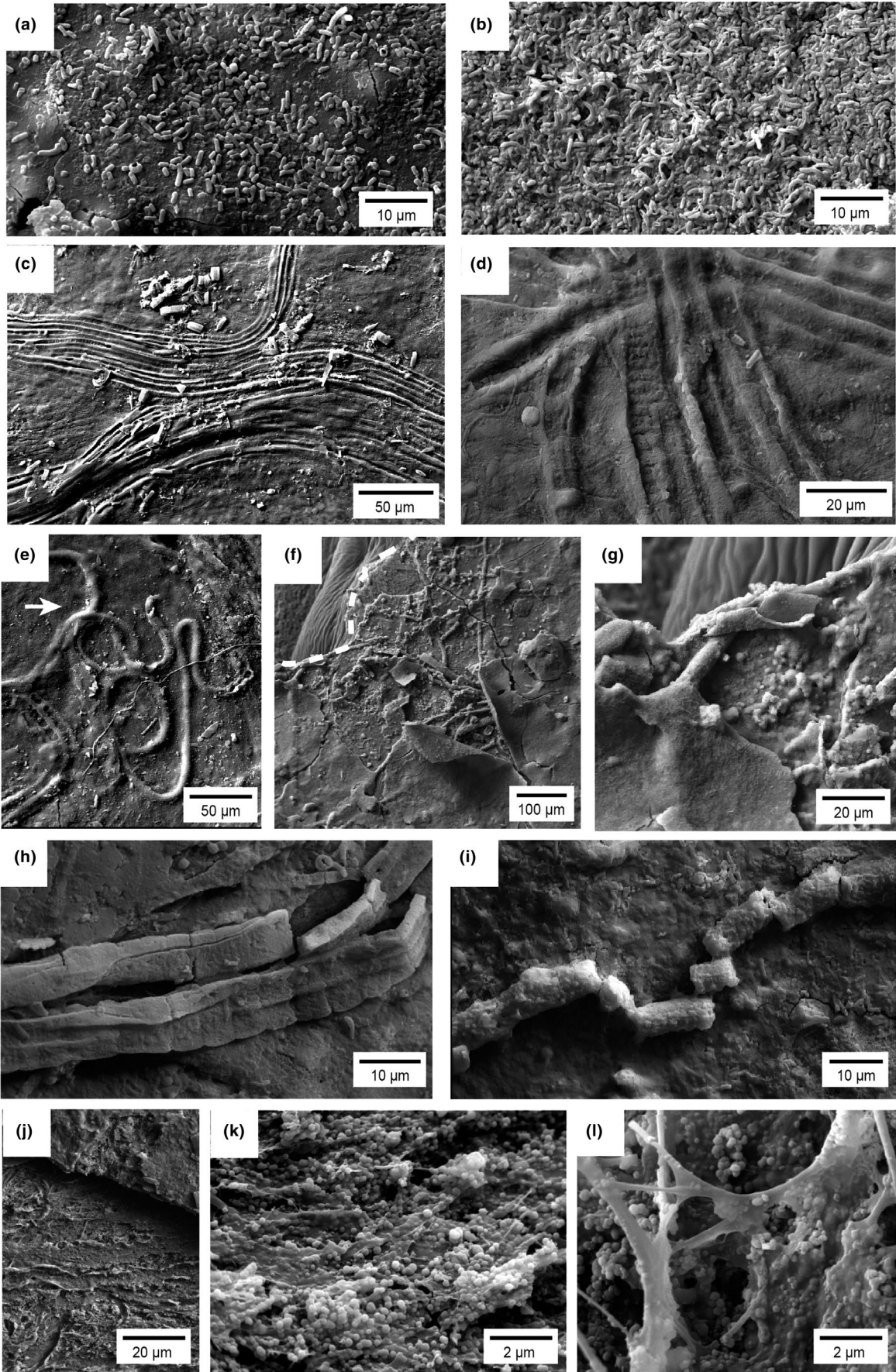
Two olive mat samples were collected for community analysis within the center of floating Vicuna Stream mats (39.3°C): (1) an unsilicified area and (2) an adjacent silicified crust and the upper green portion of the underlying olive mat (Figure 5b, Table 1). The distribution of metabolic guilds, aerotolerances, and community composition is similar in each sample, with slight differences in relative abundances of major taxa. As in the orange mats, aerobic

non-fermenting heterotrophs are the major metabolic division found in olive mats, comprising ~60% of the total community and dominated by Planctomycetes (Figure S1, Table S2). The dominant Cyanobacteria in the olive mats are filamentous *Leptolyngbya* sp. (1.6% and 2.0%) in the unsilicified and encrusted mats, respectively. Unsilicified olive mats contain the largest proportion of aerobic, anoxygenic phototrophs seen in any Vicuna Stream sample, with an even dominance between the Alphaproteobacterium *Porphyrobacter* sp. (1.9%), and *Chloroflexus* sp. (1.8%) of Phylum Chloroflexi, which is found consistently throughout El Tatio at sites with a range of temperatures and chemical compositions (Engel et al., 2013; Fernandez-Turiel et al., 2005). The same taxa are present at lower abundances in the silicified olive mat sample (0.7% and 1.1%, respectively). Aerobic chemolithoautotrophs, while a minor component (1.9%–2.1%), are also more abundant in olive mats than in the other mat types (Figure S1, Table S2).

One sample of dark green mat was removed from the outer fringe (44.1°C), adjacent to flowing Vicuna Stream waters (Figure 5d). The color of these mats is due to an overwhelming abundance of oxygenic, photolithoautotrophic Cyanobacterial taxa *Arthrospira platenensis* (64.6%) (Figure S1, Table S2). In stark contrast to the orange and olive communities, the dark green mats contain only a fraction of the members performing aerobic heterotrophy (<2.0%), and instead have a higher representation of a few prominent facultatively anaerobic heterotrophs, including the second most abundant taxon in the mat, an anaerobic and fermentative heterotrophic Verrucomicrobia *Opiritatus* sp. (12.5%) (Figure S1, Table S2).

Microbial mat samples were also collected from two locations in Middle Basin Springs (Figure S2, Table S2). Both samples were taken from olive surfaces with silicifying crusts, one within warmer mat margins adjacent to stream flow (61.1°C), the other within cooler “interior” mats 20 cm away from margins (39.3°C). Cyanobacteria were notably more abundant in olive mats from Middle Basin than Vicuna Stream, with higher abundances in cooler interior mats (30%) than mat margins (15%) (Figure S2, Table S2). Unlike Vicuna Stream, cyanobacterial taxa are dominated by *Fischerella* spp., both in cooler (26.6%) and warmer mats (11%), with lesser abundances of *Leptolyngbya* sp. (3.0–4.6%). Aerobic heterotrophs were also highly abundant in interior Middle Basin mats, most notably members of Planctomycetes including *Gemmata* sp. (11.9%), and *Algisphaera agalytica* (9.3%). By contrast, warmer mat margins had the highest abundances of aerobic photoheterotrophs within any mat sampled in this study (15.9%), including Chloroflexi such as *Chloroflexus* sp. (8.1%) and *Roseiflexus* sp. (7.4%). The most abundant taxa in warmer mat margins was *Nitrospirae* (11.1%), a member of the Nitrospirae, which oxidizes nitrite into nitrate (Figure S2, Table S2).

**FIGURE 6** SEM images of silica crusts and underlying mats from Middle Basin Springs. All images represent overhead views of the tops of layers and mats. (a, b) Surficial silica crusts covered with bacilli and exhibiting minor fracturing. (c, d) Surficial crusts with cyanobacterial filament molds. Note cellular divisions preserved in d, within the central filament. (e) Cyanobacterial filaments entombed within surficial crusts, with a potential lateral branch indicative of *Fischerella*. (f, g) Plastic and brittle deformation of surficial crusts, revealing multiple silica layers containing cyanobacterial filaments. Dashed line in f = sample edge. g is a close-up of a filament from the left-hand margin of f, revealing a filament entombed in an overlying crust layer. (h, i) Surficially preserved cyanobacterial filaments. Note cellular divisions (h) and brittle fracturing (i). (j–l) Unsilicified mats underlying silica crusts, with abundant EPS (k,l) and no large cyanobacterial filaments



## 4.5 | Microstructure of silica crusts

SEM imaging of crusts on Middle Basin Springs mats reveals multiple generations of silica precipitation and cellular preservation (Figure 6). Uppermost crust surfaces are relatively smooth, and frequently preserve long microbial filaments in various stages of degradation (Figure 6). EDS spectra of crusts and preserved filaments reveal Si and O as the most abundant elements, typically followed by C, As, Na, Cl, and Fe (Figures S4–S7). By comparison, lower layers are defined by a lack of cohesive silicification, with an abundance of smaller filaments (<2  $\mu\text{m}$  in diameter) and extracellular polymeric substances (EPS) (Figure 6 j–l). The most abundant elements in mat layers underneath crusts are C and O, with minor peaks of Al and Si (Figures S4–S7). Crust deformation is mostly brittle, exhibited through surficial cracks which cross-cut through preserved microbial filaments. Thinner crusts also exhibit more plastic behavior, peeling away from fracture zones, and revealing lower layers of silica and cells (Figure 6f, g).

The most abundant cells preserved in silica crusts are 2- to 4- $\mu\text{m}$ -long bacilli (Figure 6a, b). Bacilli are straight to slightly curving in morphology, depending on cell length. Cell exteriors are typically intact, with occasional individuals exhibiting small circular pores (Figure 6a, b). When bacilli are low in abundance, underlying opal-A crusts are visible as smooth and lightly fractured surfaces underneath cells (Figure 6a). More frequently, bacilli form dense surficial populations which obscure underlying precipitates (Figure 6b). Both surficial cells and underlying silica layers are lightly fractured, although some cracking could have initiated during SEM preparation. The cellular morphology of bacilli alone is insufficient to identify a specific microbial genus, although the most abundant potential candidate in Middle Basin mats is *Chloroflexus* (Figure S2, Table S2), which has been observed in microbial sinters in El Tatio and Iceland (Fernandez-Turiel et al., 2005; Konhauser et al., 2001). Cell exteriors are typically intact, with occasional individuals exhibiting small circular pores (Figure 6a, b). When bacilli are low in abundance, underlying opal-A crusts are visible as smooth and lightly fractured surfaces underneath cells (Figure 6a). More frequently, bacilli form dense surficial populations, which obscure underlying precipitates (Figure 6b). Both surficial cells and underlying silica layers are lightly fractured, although some cracking could have initiated during SEM preparation.

Larger filamentous microbes are frequently preserved in Middle Basin silica crusts (Figure 6c–i). Filaments are typically five to ten  $\mu\text{m}$  wide and can exceed 500  $\mu\text{m}$  in length. Filament branching is extremely rare, with only one potential example observed (Figure 6e). The most likely candidates for such filaments are cyanobacteria such as *Fischerella* and *Leptolyngbya* (Figure S2, Table S2). While *Fischerella* usually exhibits lateral filament branching, in conditions above 57°C such as Middle Basin Springs (61°C), higher temperature variants are typically unbranched (Castenholz 1973; Jones et al., 2005). Both *Fischerella* and *Leptolyngbya* have previously been identified in microbial sinters, including at El Tatio (Gong et al. 2020; Jones et al., 2005; Wilmeth et al., 2020). Three filament preservation styles occur in

silica crusts: (1) entombed filaments, (2) filament molds, and (3) surficial filaments. Preservation modes are not mutually exclusive; a single filament can progress from one to another mode of preservation along its length (Figure 6g). However, individual filaments typically retain the same preservation style over hundreds of  $\mu\text{m}$  (Figure 6c).

Entombed filaments occur as linear or sinuous ridges rising out of crusts, coated in the same generation of opal-A as immediately adjacent crust surfaces (Figure 6e, g). Entombed microbes preserve the least amount of cellular detail and are frequently overlain by other filaments. In samples where multiple generations of silica crusts are observed through fracturing and peeling (Figure 6f), filaments entombed within upper silica crusts are revealed in greater detail on lower levels, showing “surficial” preservation (Figure 6g).

Surficial filaments rest directly on top of silica crusts (Figure 6h, i), as opposed to entombed filaments forming ridges covered by opal-A sheets. Surficial samples include the most detailed preservation of microbial filaments. Several filaments exhibit cellular partitioning every 2–5  $\mu\text{m}$  (Figure 6h), features that are absent in entombed filaments, and less well-preserved in filament molds (Figure 6d). Most filaments are intact, although some exhibit brittle deformation, having fractured and separated into segmented cylinders (Figure 6i). Diatoms up to 50  $\mu\text{m}$  long are also surficially preserved and are not observed as molds or entombed frustules.

A sharp boundary exists between silica crusts (1- to 2-mm-thick) and underlying mats in the Middle Basin Springs (Figure 6J). Several distinguishing features of crusts are absent in lower mats (Figure 6j–l), including smooth opal-A surfaces, microbial filaments wider than two  $\mu\text{m}$ , and abundant bacilli. Instead, mats below 2 mm depth are composed of isolated spherules between 250 nm and 1  $\mu\text{m}$  in diameter. Spherules occur on uneven surfaces of EPS, which frequently branch and interlink between thin filaments up to 2  $\mu\text{m}$  long (Figure 6k–l). EDS analysis of spherules reveals abundant Si and O, with slightly more abundant proportions of C than overlying crusts (Figures S4–S7). Some spherules are therefore opal-A precipitates, although the EDS data do not exclude the potential for some spherules to represent coccoidal microbial cells, as both features can share the basic morphology and size. No gradation appears to exist between overlying crusts and underlying mat textures (Figure 6j). Thin filaments (<2  $\mu\text{m}$ ), EPS, and spherules are not observed in crusts, and larger filaments are not present in underlying crust-free mats.

## 4.6 | Microelectrode profiles of microbial mats

Two series of microelectrode profiles were measured within Vicuna Stream mats (Figures 7, 8). Both series divide mats into three physical zones based on subaerial exposure and silicification (see Section 4.3 for more detailed physical descriptions): (1) subaqueous mats, (2) subaerial mats, and (3) encrusted mats.

The first microelectrode profile series was taken 1.5 m downstream from Vicuna Stream's source, within mats proximal to the eastern stream bank (Figure 7a), on a 2-cm transect starting in orange subaqueous mats, progressing outward to unsilicified olive

subaerial mats, and ending with olive subaerial mats with silica crusts. All three zones were profiled for  $O_2$  concentrations and pH in quadruplicate runs, with each new profile taken 1 mm downstream from the previous measurement (Figure 7).  $O_2$  concentrations ( $[O_2]$ ) under subaqueous mats and subaerial mats without crusts peaked around 0.6 mM (Figure 7). In subaqueous mats, maximum  $[O_2]$  occurred between 4 and 5 mm depth and reached 0 mM between 8 and 10 mm depth (Figure 7b). Oxygen profiles in subaerial mats were confined closer to the surface, peaking between 3 and 4 mm, and diminishing to 0.1 mM by 7 mm depth (Figure 7c). Profiles of pH in both mats were almost identical, reaching maximum values  $\sim 8.8$  at 2 mm depth, and returning to stream values of 6.8 by 5 mm depth. Subaerial mats with silica crusts had notably different  $[O_2]$  and pH profiles than the unsilicified mat textures (Figure 7D). Values of  $[O_2]$  never exceed 0.4 mM and peak in the first 3 mm, with one exception at 8 mm depth. No pH profile under silica crusts exceeded values of 7.8, with three profiles peaking at 3 mm depth.

The second microelectrode profile series was taken 1 m downstream from Vicuna Stream's source as an 18 cm transect of  $O_2$  and pH (Figure 8), from orange submerged mats through olive mats with various levels of exposure and silicification, ending within dark green subaqueous fringes on the mat's distal edge. Profiles under all three surfaces showed similar trends to the smaller-scale survey, with greater variability due to larger distances covered (Figure 8C). Under subaqueous mats,  $[O_2]$  peaked between 4 and 5 mm depth. Peak  $[O_2]$  values and corresponding depths in mats increased with distance from shore, from 1 mM at 2.5 mm depth in proximal orange mats, to 1.2 mM at 4 mm depth in olive mats, to over 2 mM at 5 mm depth in dark green distal fringes, the highest observed in this study (Figure 8b, c). Distal green fringes also had the most alkaline pH values of any mat profile, gradually reaching 10.2 at 7 mm depth before sharply dropping back to 6.8 at 9 mm. Distal pH profiles differed greatly from proximal orange and olive mats, which peaked at 8.8 within 2 mm depth.

Subaerial mats with no crust had diminished  $[O_2]$  profiles compared with subaqueous mats (Figure 8c), with maximum values varying between 0.3 and 0.6 mM. Profiles did not show trends with stream bank distance, with olive mats at 12 cm along the transect showing maximum  $[O_2]$  values at 2 mm depth. Mats at 12 cm also produced a pH profile unlike any unsilicified mat, decreasing at 3 mm depth before slowly increasing to 8.3 at 12 mm depth. The discrepancy between  $[O_2]$  and pH profiles in this sample could be related to adjacent silica crusts, as pH patterns more closely resemble the erratic shifts underneath silicified zones (Figure 8a). Other subaerial pH profiles maintained consistent shape, peaking slightly deeper than subaqueous mats (7.7 at 2.5 mm depth).

As observed in the first microelectrode profile series,  $[O_2]$  patterns were lowest underneath silica crusts, never exceeding 0.5 mM (Figure 8c). The peak values and extent of relative  $[O_2]$  maxima diminished with increasing distance from shoreline. Profiles under crusts closest to shore remained steady at 0.4 mM  $O_2$  until 5 mm, while middle crusts were only 0.4 mM in the top millimeter, and distal crusts never exceeded 0.2 mM  $O_2$ . Maximum pH values

underneath crusts never exceeded 8.3, in contrast with subaqueous ( $pH > 10$ ) and subaerial mats ( $pH = 8.9$ ). Most notably, shallow mats under middle crusts (14 cm along the transect) were more acidic than any other Vicuna Stream mat ( $pH = 5.5$ ), before rapidly increasing to values of 8 within 1 mm (Figure 8c).

## 5 | DISCUSSION

Silica solubility in hydrothermal microbial mats is governed by multiple parameters including water temperature, evaporation, and pH (see review in Fournier, 1985). Different parameters are influenced by downstream chemical gradients, the physical properties of microbial mats, and chemical changes due to microbial metabolisms. Conversely, progressive silicification within a microbial mat has the potential to influence the physical properties and metabolic processes of the affected ecosystem. Examining the variations of environmental parameters, surficial textures, and metabolic responses within Vicuna Stream mats therefore provides a unique opportunity to examine the relationship between environmental chemistry and microbialite preservation.

### 5.1 | Silica solubility and temperature

Silica concentrations in Vicuna Stream range between 102 and 140 ppm  $SiO_2$  (48–65 ppm Si, 1.8–2.3 mM Si) and decrease downstream (Figure 4). Such values are within previously measured distributions from various locations in El Tatio, although maximum silica concentrations in Vicuna Stream are notably lower than other studies (205 ppm, Cortecci et al., 2005; 219 ppm, Fernandez-Turiel et al., 2005; 310 ppm, Phoenix et al., 2006). Maximum water temperatures are also lower in Vicuna Stream (52.6°C) compared with prior geochemical analyses (77°C, Cortecci et al., 2005; 86°C, Phoenix et al., 2006). Lower silica concentrations and temperatures in Vicuna Stream are most easily explained by dilution from cooler waters upstream from the primary hydrothermal pool. In contrast, previously measured geochemical data from El Tatio primarily comes from geysers, hot springs, and pools with lower influence from surficial waters (Cortecci et al., 2005; Phoenix et al., 2006).

The effects of temperature on silica solubility are well constrained by experimental data and models (Gunnarsson and Arnórsson 2000). Silica solubility decreases in cooling solutions, driving conditions toward supersaturation and potential opal-A precipitation. While daytime Vicuna Stream temperatures grow cooler with distance from the hydrothermal pool, silica concentrations decrease along the same transect and prohibit silica supersaturation, even though conditions are between 80% and 90% saturation at ambient pH values of 6.8 (Figure 4). Water temperatures are consistently higher on streambeds several cm below microbial mats, producing more silica-undersaturated solutions (Figure 4).

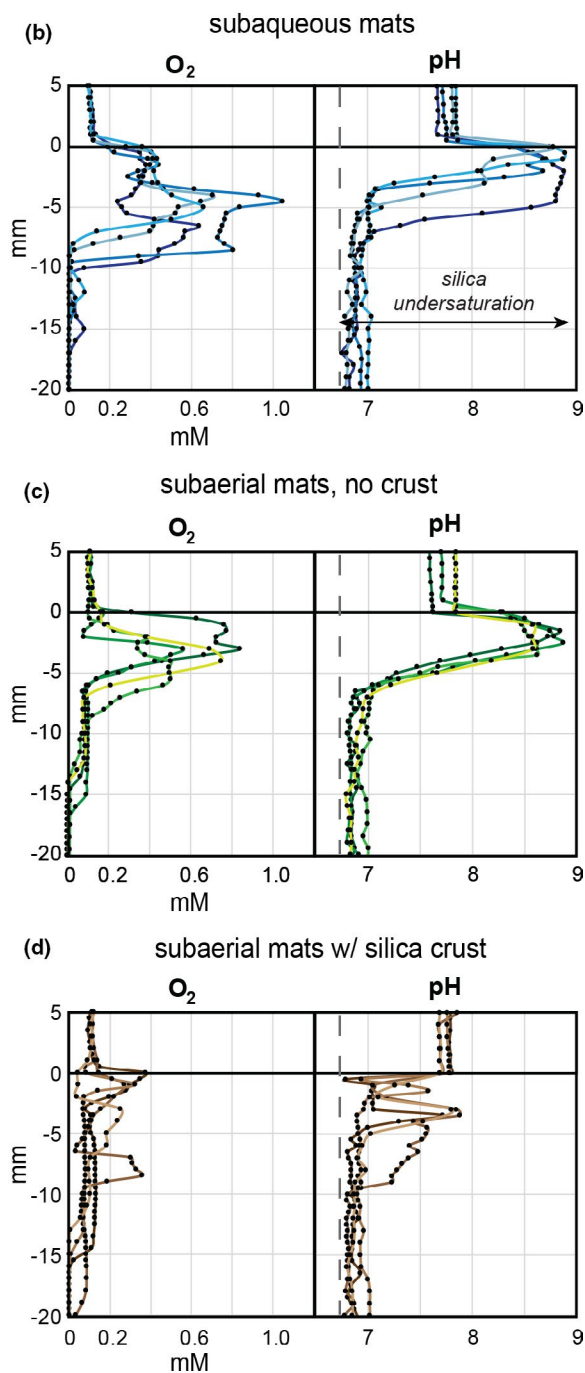
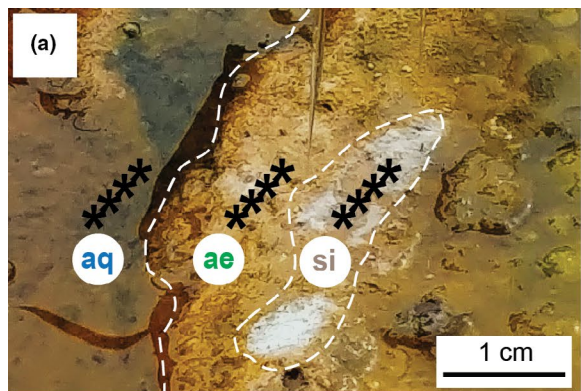


**FIGURE 7** Quadruplicate microprofiles of  $O_2$  and pH from floating Vicuna Stream mats, 1.5 m downstream (see Figure 2c for location). Stars represent replicate profile locations, spaced 1 mm apart parallel to stream flow. Distances between sampling locations in subaqueous (aq), subaerial (ae), and encrusted mats (si) is 1 cm, perpendicular to stream flow. Note the diminished  $O_2$  and pH profiles in silica-encrusted mats compared with unsilicified mats

Within mats 1.3 m downstream from the primary hydrothermal source, surface stream temperatures fell from peak daytime values of 40–45°C to 25–30°C at night, driving amorphous silica precipitation from solutions at or above 130 ppm  $SiO_2$ . Stream temperatures remained relatively constant for 12 h as overlying air temperatures dropped below freezing. Warmer waters at the base of the same mats (~15 cm deep) were only measured at peak afternoon temperatures (45°C). If the lower portions of mats cooled by the same amount as shallow waters (10–20°C), the entire mat at 1.3 m downstream would become silica-supersaturated at night; it is possible that deeper mat layers experienced less severe temperature shifts. In either case, silica precipitates were only observed in surficial crusts, not at the base of microbial mats.

Nighttime temperatures were not measured in other downstream mats. However, considering the relative stability of measured nighttime water temperatures, and evidence for downstream hydrothermal sources in Vicuna Stream (Figure 4), this study conservatively assumes nighttime surficial temperatures in most downstream mats to be no higher than 25–30°C within our observation time-frame. At such temperatures, most surficial mats would theoretically become silica-supersaturated at night, although it is possible that warmer areas due to secondary hydrothermal input (e.g., 4 m downstream) experience more frequent periods of undersaturation.

## 5.2 | Evaporation and silica precipitation

High evaporation rates at El Tatio (~131.9 mm/month, Nicolau et al., 2014) are fostered by relatively low humidity and high wind speeds on the Chilean Altiplano, and both frequently factor into local silicification models (Fernandez-Turiel et al., 2005; Munoz-Saez et al., 2018; Nicolau et al., 2014; Slagter et al., 2019; Gong et al., in review). Elsewhere in the Upper Basin, long-term experiments have measured evaporative silica precipitation rates on abiotic surfaces such as glass slides (Nicolau et al., 2014). Those authors observed thin, layered silica deposits (200  $\mu\text{m}$ –2 mm thick) forming within several days on surfaces near the air–water interface. They also found no significant change in precipitation rates along cooling gradients, although the lowest temperatures measured (57°C) are notably higher than the warmest waters in Vicuna Stream (Figure 4). The study also noted that microbial mats could potentially modulate silicification rates by supplying various substrates such as cells and EPS as nuclei for precipitation.

Silicifying mats floating in Vicuna Stream and other locations in El Tatio provide a unique comparison with previous evaporation experiments. In Vicuna Stream waters, the most undersaturated solutions with respect to silica are still 80%–90% saturated (Figure 4). In such conditions, only 10%–20% evaporation of a given solution is required before reaching supersaturation, with increasing potential for silica precipitation as evaporation continues. In contrast, evaporation experiments performed by Nicolau et al. (2014) occurred in warmer waters (147 ppm  $\text{SiO}_2$ , ~82°C) only 50% saturated in silica, requiring half of a given water volume to evaporate before potential opal-A precipitation. The same study did not measure subsequent silica concentrations in downstream evaporation experiments, but assumed undersaturation throughout the profile. The higher relative saturation state at lower silica concentrations in Vicuna Stream waters is likely due to silica-rich hydrothermal fluids immediately interacting with cooler surficial waters.

While direct measurements of evaporation and silica precipitation rates were not feasible in this study, two environmental parameters were analyzed to qualitatively assess diurnal cycles of evaporation at Vicuna Stream: relative humidity and wind speed (Figure 3b). Early afternoons are the most optimal conditions for evaporation, with the lowest average humidity (20%–30%) and wind speeds up to 5 m/s. By contrast, lower wind speeds and relative humidity above 70% after sunset were less likely to facilitate evaporation. Therefore, two primary influences on silicification at Vicuna Stream alternate on diel cycles, with silica supersaturation dominated by evaporation in daylight, and by cooling water temperatures at night. Furthermore, evaporation is the most likely candidate to foster silica precipitation on surfaces of Vicuna Stream mats where temperature and pH alone are insufficient factors.

### 5.3 | Effects of silicification on oxygenic photosynthesis

Between 15% and 30% of the microbial community in encrusted mats from Middle Basin Springs is composed of Cyanobacteria, dominated by the branching filamentous taxa *Fischerella* (Figure S2). Samples from Middle Basin Springs contain the highest cyanobacterial abundances from floating mats in El Tatio (Figure S2), only surpassed by the unsilicified, *Arthrospira*-dominated green mat fringes in Vicuna Stream. Mat fringes at Middle Basin Springs represent the warmest environment collected in this study (61.1°C). Here, abundances of Cyanobacteria are roughly equivalent with anoxygenic photosynthesizers such as *Chloroflexi*.

In contrast, cyanobacterial abundances in Vicuna Stream are below 5% and feature *Leptolyngbya* sp. (Figure S1), which is also prevalent in Middle Basin Springs and dominates preserved microbial palisade sinters elsewhere in El Tatio (Gong et al. 2020). Cyanobacterial abundances are similar between olive mats with and without silica crusts in Vicuna Stream, indicating that the process of silicification does not greatly affect the proportion of cyanobacteria in a given community. Furthermore, the similarities in the

macroscopic textures of surficial crusts on Middle Basin Springs and Vicuna Stream communities indicate that crust formation does not depend on specific microbial taxa.

Despite the relatively low abundance of cyanobacteria in Vicuna Stream, pH and  $\text{O}_2$  profiles in unsilicified mats (Figures 7, 8) are nearly identical to profiles measured in cyanobacterial mats from various environments (Jorgensen et al., 1983; Revsbech et al., 1983; Epping & Kuhl, 2000; Wieland and Kuhl 2000). Elevated  $\text{O}_2$  concentrations (>0.8 mM) and pH values above 8 within the top 5 mm of Vicuna Stream mats are classic signatures of oxygenic photosynthesis performed by cyanobacterial communities (Jorgensen et al., 1983; Revsbech et al., 1983; Epping & Kuhl, 2000; Wieland and Kuhl 2000).

Profiles of pH and  $\text{O}_2$  are both diminished underneath silica crusts in Vicuna Stream mats, and more closely resemble previously measured profiles in cyanobacterial mats during nighttime or dark experiments (Kuhl et al., 1996; Revsbech et al., 1983). While opal-A can reflect or absorb a significant portion of solar radiation, a significant fraction of light can still be transmitted through thin silica surfaces (Phoenix et al., 2001). The light-absorption properties of siliceous precipitates at El Tatio were previously measured by Phoenix et al. (2006) who noted that photosynthetically active radiation (PAR) was less attenuated through crusts than ultraviolet radiation, especially UV-B and UV-C. El Tatio silica crusts of equivalent thickness to Vicuna Stream samples (1.4 mm) absorbed 78%–92% of PAR, and between 93 and 100% of UV-B and UV-C (Phoenix et al., 2006). During our observation window at Vicuna Stream, the maximum solar irradiance was 80,000 lux at 14:00 hours (Figure 3). Under such conditions, PAR in mats below silica crusts would theoretically be <0.64 lux.

While crusts at Vicuna Stream potentially remove up to 90% of incoming PAR, the resulting light levels are not inhibitive of oxygenic photosynthesis. Experimental studies on cyanobacterial mats in low-light conditions observed little to no difference in maximum  $\text{O}_2$  concentrations (0.6–1.0 mM) and pH values (8–9) at various irradiances between 2000 and 4400 lux (Al-Najjar et al., 2012; Epping & Kuhl, 2000; Pringault et al., 2005; Lichtenberg et al., 2017; Wieland and Kuhl 2000). Elsewhere in El Tatio, photosynthetically active cyanobacterial communities occur up to 1 cm deep in siliceous sinters, at even lower light levels than under Vicuna Stream crusts. Therefore, decreased irradiance alone cannot sufficiently explain diminished pH and  $[\text{O}_2]$  profiles under silicified Vicuna Stream mats.

The key difference between darkened mats in Vicuna Stream and many irradiance experiments, including within more highly lithified El Tatio sinters, is the temperature of the respective microbial communities. Previous studies have shown that cyanobacterially dominated mats in waters above 30°C require more light to achieve local oxygen concentrations above 0.4 mM (Epping & Kuhl, 2000; Wieland and Kuhl 2000). For instance, Epping & Kuhl, 2000 observed that at 30°C, mats from the Ebro Delta in Spain required irradiances of 22,000 lux ( $500 \mu\text{mol} \cdot \text{m}^{-2} / \text{s}$ ) or greater to produce local  $\text{O}_2$  concentrations above 0.2 mM. At irradiances of equivalent to conditions below El Tatio silica crusts (5000 lux =  $118 \mu\text{mol} \cdot \text{m}^{-2} / \text{s}$ ),

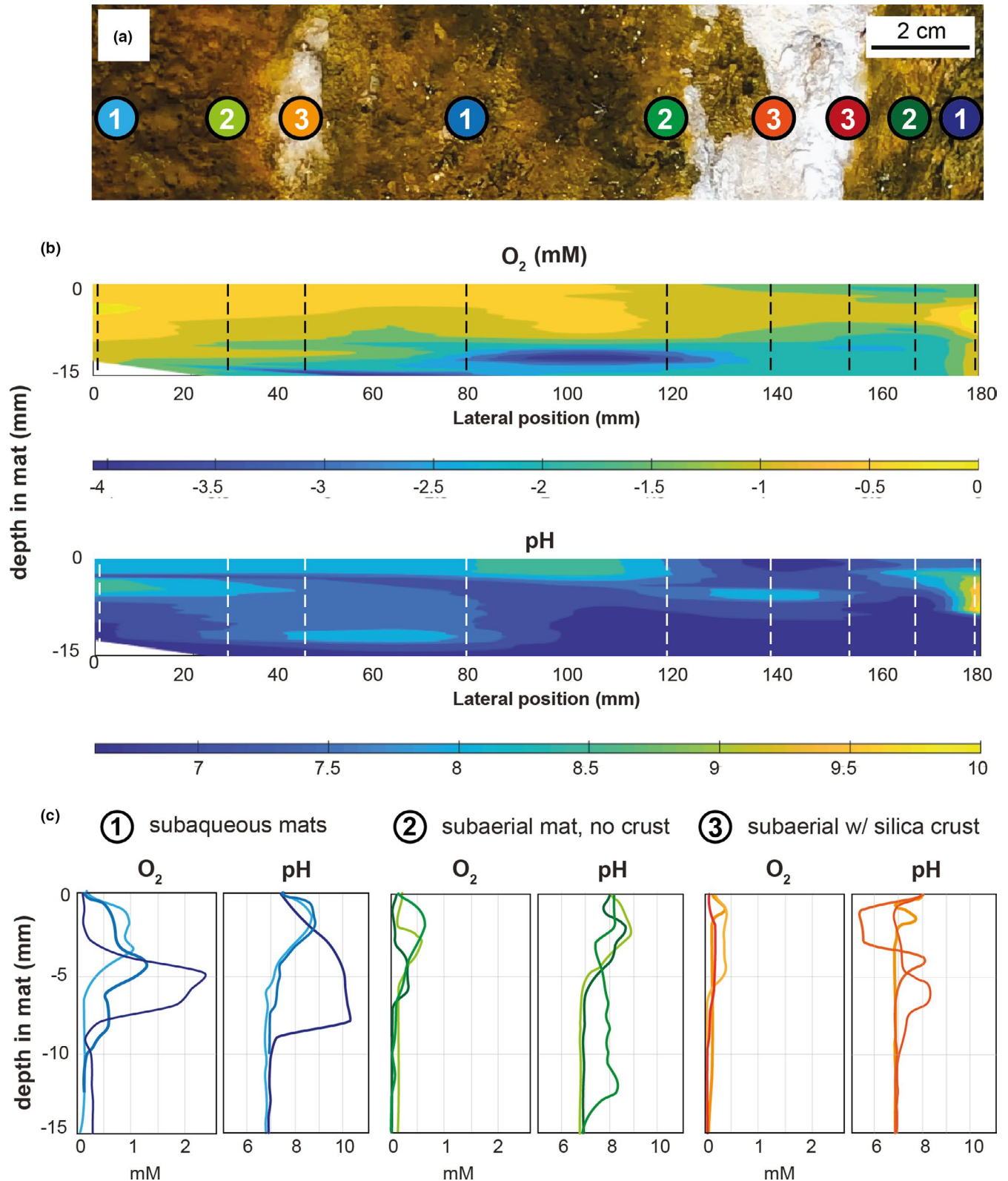


**FIGURE 8** Microprofile transect of  $O_2$  and pH from floating Vicuna Stream mats, 1 m downstream (see Figure 2C for location), taken perpendicular to stream flow. (a) Overhead view of mat transect. Numbered circles represent subaqueous (1), subaerial (2), and encrusted mats (3), with lighter colors toward stream margins. (b) Modeled  $O_2$  and pH transect, representing a cross-section beneath mat surfaces up to 15 mm depth. (c) Individual microprofiles. Colors in (a) correspond to profiles in (c). Note the diminished  $O_2$  and pH profiles in silica-encrusted mats compared with unsilicified mats, and the intermediate  $O_2$  production in subaerial, unsilicified mats

O<sub>2</sub> profiles in Ebro mats at 30°C were nearly identical to profiles measured in complete darkness (Epping & Kuhl, 2000). While similar temperatures and light levels did not inhibit peak O<sub>2</sub> concentrations (0.7 mM) in warmer mats from Solar Lake, Israel, temperatures at 40°C diminished maximum O<sub>2</sub> concentrations to 0.4 mM at 5000 lux irradiance (Wieland and Kühl 2000). The temperature, light levels, and maximum local O<sub>2</sub> concentrations in the Solar Lake experiments are nearly identical to the same parameters in Vicuna Stream mats when placed under light-attenuating silica crusts (Figures 4, 7, 8). As shown in Figure 8 at ~40°C, Vicuna Stream mats without crusts attain concentrations of more than 1 mM O<sub>2</sub>, while immediately adjacent encrusted mats only produce up to 0.4 mM O<sub>2</sub>. In situ measurements from Vicuna Stream not only corroborate previous experiments linking temperature and light levels to photosynthetic oxygen production within microbial mats, but also provide the first description of silica precipitation inhibiting oxygenic photosynthesis within microbial mats.

#### 5.4 | Silica solubility and pH

This study reveals large shifts in pH with depth through the mats (Figures 7, 8), as typically observed in previous studies of microbial mats undergoing oxygenic photosynthesis (Jorgensen et al., 1983; Revsbech et al., 1983; Epping & Kuhl, 2000; Wieland and Kühl 2000). Oxygenic photosynthesis within the top five millimeters of unsilicified mats produces more alkaline solutions, with an average maximum of 8.8 and one measurement above pH 10 (Figures 7, 8). In contrast, Vicuna Stream mats with silica crusts and diminished oxygenic photosynthesis had lower average pH (~7.5) than unsilicified textures, with only one profile briefly exceeding pH 8 (Figures 7, 8). Variations in pH within Vicuna Stream mats effect SiO<sub>2</sub> solubility and the potential to precipitate silica. The positive relationship between silica solubility and pH is non-linear (Alexander et al., 1954), with much higher silica concentrations needed to saturate solutions above pH 8–9 (Table S3) because at pH values above 9, silicic acid deprotonates and drives amorphous silica dissolution [Reaction 1] (Alexander et al., 1954).



As described in Section 5.1, ambient pH values of 6.8 in Vicuna Stream waters are silica-undersaturated at daytime temperatures, while nighttime cooling favors silica precipitation in most mats (Figure 4, Table 1; Table S2). The relative degree of silica undersaturation can be calculated by dividing the measured SiO<sub>2</sub> concentrations by the solubility concentration at the same temperature and pH.

At maximum solar irradiance (8 lux) and water temperatures (~45°C) during early afternoons in Vicuna Stream, silica solubility was 176 ppm SiO<sub>2</sub> in surficial unsilicified mats 1.3 m downstream (pH 8.8) and 148 ppm SiO<sub>2</sub> under adjacent mats with silica crusts (pH 7.5) (Table S3). At measured SiO<sub>2</sub> concentrations of 132 ppm, unsilicified

mats in the same location were therefore 75% silica-saturated, while mats under silica crusts were 89% saturated. All mat surfaces are undersaturated during this period of time, although conditions under crusts are slightly less favorable for silica dissolution than adjacent mats without crusts. The presence of crusts therefore produces areas of microbial mats that have lower pH values, lower oxygen concentrations, and are more silica-saturated than surrounding mats without crusts. Differences in silica saturation within mats over time could potentially impact the stability of overlying crusts, but such hypotheses require longer-term observations to validate.

One notable pH outlier occurred within an encrusted mat profile farthest from the Vicuna Stream bank (Figure 8c). From 1 to 3 mm depth, the mat pH dropped to 5.5, more than one unit lower than any other observed values. However, due to the non-linear solubility trends of silica with respect to pH, silica solubility of 146 ppm SiO<sub>2</sub> at pH 5.5 is equivalent to ambient stream waters at pH 6.8 at temperatures between 0 and 100°C (Table S3). Since mat profiles were not measured at night, it remains unknown whether such acidic conditions are typical in darkened Vicuna Stream mats. The absence of similarly low pH values under six other Vicuna Stream crusts (Figures 7, 8), and within many previous light-dark studies of cyanobacterial mats (Epping & Kuhl, 2000; Jorgensen et al., 1983; Revsbech et al., 1983; Wieland and Kühl 2000), indicates that such acidic excursions are potentially rare, although the hypersaline nature of some of previously studied systems could also buffer against the same excursions (Jorgensen et al., 1983; Revsbech et al., 1983).

#### 5.5 | Preservation potential of mats in low-silica solutions

Microbial mats with silica crusts in Vicuna Stream and Middle Basin Springs represent an intermediary stage between unmineralized microbial communities and lithified sinter deposits. Up to 75% of floating mat surfaces are covered with brittle crusts (Figure 2b) composed of silica as confirmed by EDS spectra (Figures S4–S7), but fully silicified sinters are not present at either location. By contrast, lithified sinters frequently occur around geothermal pools, geysers, and streams elsewhere in El Tatio (Fernandez-Turiel et al., 2005; Gong et al. 2020, in review; Jones & Renaut, 1996; Munoz-Saez et al. 2016, 2015; Nicolau et al., 2014; Phoenix et al., 2006). The absence of such sinters within or adjacent to floating El Tatio mats is most likely due to silica-undersaturated source waters with relatively low dissolved SiO<sub>2</sub> (<150 ppm) (Figures 4, 9). In geothermal locations around the world (including elsewhere in El Tatio), subaerial sinter formation occurs in solutions with [SiO<sub>2</sub>] >200 ppm, while subaqueous sinters form in solutions >300 ppm SiO<sub>2</sub> (Figure 9).

The partially encrusted mats in Vicuna Stream and Middle Basin Springs most closely resemble cyanobacterial communities from downstream waters in Octopus Spring (50°C, pH = 7.5) in Yellowstone National Park (Hinman & Lindstrom, 1996). As evaporation progresses on mat surfaces in Octopus Spring, capillary forces pull water upward through porous microbial layers, providing

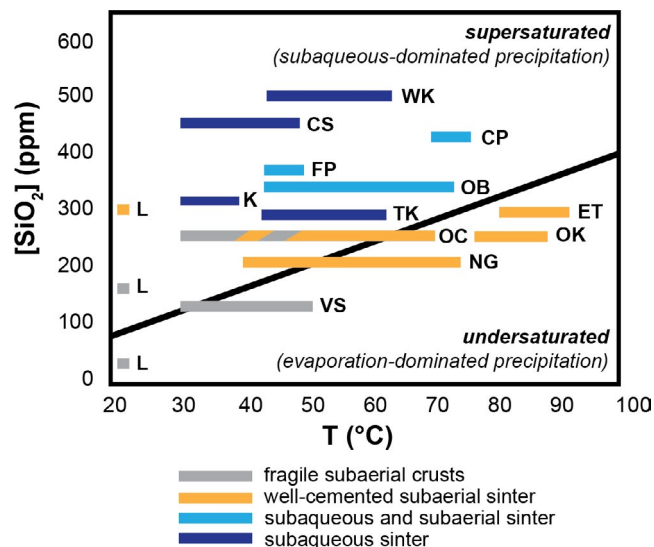


**FIGURE 9** Sinter precipitation patterns in thermal waters at different saturation states, adapted from Mountain et al. (2003). The black line represents amorphous silica solubility at pH = 7 (Gunnarsson & Arnórsson, 2000). References and pH values for each location are listed in Table S4. CP: Champagne Pool, New Zealand; CS: Cistern Spring, Yellowstone, USA; ET: various El Tatio springs, Chile; FP, Frying Pan Lake, New Zealand; K: Krysuvik, Iceland; L: laboratory evaporation experiments, Orange et al., 2018; OB: Obsidian Pool Prime, Yellowstone, USA; OC, Octopus Spring, Yellowstone, USA; OK: Orakei Korako, New Zealand; TK, Tokaanu, New Zealand; VS: Vicuna Stream, Chile (this study); WK: Wairakei, New Zealand.

a continuous source of  $\text{SiO}_2$  to evaporate, saturate, and eventually precipitate silica as thin surficial crusts, a process defined as “capillary creep” or “wicking” (Hinman & Lindstrom, 1996). We propose a similar wicking process for floating mats at El Tatio: Subaerial exposure of mat surfaces to arid and windy conditions enhances evaporation and capillary transport of silica-rich waters to mat surfaces. However, dissolved  $\text{SiO}_2$  concentrations are significantly higher in Octopus Spring (180–300 ppm) than in Vicuna Stream (100–150 ppm) (Figure 9), allowing cementation to transform fragile crusts into more durable sinter deposits (Hinman & Lindstrom, 1996). Similar dichotomies in silica precipitation and  $\text{SiO}_2$  concentration are also observed in laboratory experiments, where silica deposits produced by evaporating 30 and 150 ppm  $\text{SiO}_2$  solutions result in porous, friable crusts (Figure 9), while evaporating 300 ppm solutions produced denser, thicker deposits (Orange et al., 2018). Similarly, wicking and evaporation can produce a variety of well-cemented subaerial sinters in solutions over 200 ppm  $\text{SiO}_2$ , not only in undersaturated solutions such as Ngatamariki and Orakei Korako in New Zealand (Campbell et al., 2002; Lynne et al., 2019; Mountain et al., 2003) and various high-temperature springs elsewhere in El Tatio (Jones & Renaut, 1997; Nicolau et al., 2014) but also in supersaturated locations such as Champagne Pool in New Zealand (Handley et al., 2005, 2008). In silica-undersaturated hydrothermal springs, higher dissolved  $\text{SiO}_2$  concentrations permit cementation

and vertical sinter growth via evaporation, while lower concentrations in locations such as Vicuna Stream prevent evaporative crusts from progressing into well-cemented sinter deposits (Figure 9).

Silica deposits are not observed within submerged benthic mats or below floating mat surfaces in Vicuna Stream or Middle Basin Springs, and SEM images reveal a sharp decrease in opal-A beneath crusts in Middle Basin Springs (Figure 6j-l; Figures S4–S7). Such observations are consistent with silica-undersaturated conditions measured in Vicuna Stream (Figure 4), and with previously observed patterns of subaqueous sinter deposition in other geothermal locations (Figure 9). Subaqueous sinter formation is only observed in supersaturated conditions above ~300 ppm  $\text{SiO}_2$  (Figure 9), typically forming stromatolitic deposits (Berelson et al., 2011; Guidry & Chafetz, 2002; Jones et al., 2005; Konhauser et al., 2001; Mountain et al., 2003). Subaerial sinter formation can co-occur alongside subaqueous silica precipitation (Figure 9); in such cases, evaporation forms spicules or flat layers on top of submerged sinter deposits (Berelson et al., 2011; Handley et al., 2005, 2008; Jones et al., 2005; Mountain et al., 2003). In contrast, the undersaturated, low-silica conditions in Vicuna Stream and Middle Basin Springs inhibit both subaqueous and subaerial sinter formation. While recent laboratory experiments have observed opal-A precipitation in silica-undersaturated cyanobacterial mats, most likely due to cation-bridging on  $\text{Mg}^{2+}$  ions bound within EPS (Moore et al., 2020, 2021), such processes appear to be insufficient to form well-cemented subaqueous sinters in observed El Tatio mats.

The lack of durable, well-cemented silica deposits in Vicuna Stream and Middle Basin Springs greatly reduces the long-term preservation potential of the floating encrusted mats, as opposed to siliceous sinters and stromatolites in other hydrothermal locations, which are frequently compared with ancient deposits as old as 3.5 Ga (Berelson et al., 2011; Djokic et al., 2017; Jones et al., 2005; Konhauser et al., 2003; Trewin et al., 2003; Walter et al., 1996; Wilmeth et al., 2019). While geothermal sinters are not directly analogous to many siliceous stromatolite localities in the rock record, global patterns of sinter precipitation (friable crusts vs. subaerial sinters vs. subaqueous sinters) from locations with various temperatures and pH ranges indicate that microbial communities in solutions at or above 200 ppm  $\text{SiO}_2$  are more likely to become preserved in the rock record (Figure 9). More specifically, in conditions below ~200 ppm  $\text{SiO}_2$ , microbial mats form thin siliceous crusts under evaporative conditions, but are unlikely to progress into microbial sinter deposits. In most environments with concentrations between 200 and 300 ppm  $\text{SiO}_2$ , evaporation is sufficient to produce subaerial sinters via wicking and capillary action, and subaqueous stromatolites do not typically form (Figure 9). Finally, both subaqueous stromatolites and evaporative subaerial sinters will form in solutions over ~300 ppm  $\text{SiO}_2$  (290 ppm for Tokaanu, New Zealand, Mountain et al., 2003).

Patterns of subaqueous and subaerial sinter precipitation in modern hydrothermal systems could help provide estimates of  $\text{SiO}_2$  concentrations for ancient sinter deposits (Djokic et al., 2017; Konhauser et al., 2001; Lynne et al., 2008; Walter et al., 1996;

Wilmeth et al., 2019). Locations that contain extensive stromatolitic subaqueous sinters are more likely to form in conditions above 300 ppm  $\text{SiO}_2$ . Further investigations into partially silicified mats and silica-undersaturated environments could also constrain depositional and geochemical models behind ancient microbial silicification in non-hydrothermal deposits (Manning-Berg & Kah, 2017; Moore et al., 2020, 2021; Wilmeth et al., 2018). For example, the relationship between evaporative sinter preservation and silica concentrations can be compared with previous models of evaporative silicification and the chemical composition of Proterozoic peritidal mats (Manning-Berg & Kah, 2017).

Patterns of cellular preservation in El Tatio mat crusts potentially indicate selective preservation of microbial taxa. SEM images reveal two cellular morphologies abundantly preserved within siliceous crusts: (1) large filaments interpreted as cyanobacteria, potentially *Fischerella* and *Leptolyngbya* (Figure 6c-i), and (2) smaller curved bacilli tentatively interpreted as members of Phylum Chloroflexi (Figure 6a, b). Other taxa in silicifying mats from Middle Basin springs and Vicuna Stream comprise a diverse assemblage of metabolisms (aerobic and anaerobic respiration, fermentation, chemolithoautotrophy, etc.) and phyla (Proteobacteria, Planctomycetes, Bacteroidetes, etc.). Such taxa could be represented in unsilicified microbial communities deeper within mats, which contain cellular textures absent in overlying crusts, including coccoids and thinner filaments (Figure 6j-l). Crust formation alone does not appear to impact the overall diversity of silicifying microbial communities, as adjacent mats with and without crusts contain similar proportions of taxa and metabolic guilds (Figure S1B). Therefore, different patterns of cell morphologies observed in SEM images within and below crusts are potentially due to vertical shifts in community composition, with taxa in the uppermost surficial layers more likely to become preserved during evaporation. Further analyses of microbial metabolisms and cellular textures at different depths in silicifying mats will provide a more complete understanding of selective cellular preservation in silica beyond phototrophic clades such as Cyanobacteria.

Regarding patterns of silicification and oxygenic photosynthesis, previous experiments in undersaturated solutions (21°C, 15–100 ppm  $\text{SiO}_2$ ) indicate that photosynthetically active cyanobacterial mats precipitate higher quantities of amorphous silica than inactive mats (Moore et al., 2020, 2021). While such results differ from observed patterns in El Tatio mats (diminished silica precipitation within photosynthetically active mats), the two datasets are not incompatible. Silica precipitation in previous experiments was primarily driven by cation-bridging to  $\text{Mg}^{2+}$  cations bound within EPS produced by active mats (Moore et al., 2020, 2021). Mg concentrations were not measured in this study but are typically orders of magnitude lower than silica concentrations in El Tatio springs (0.2–2 ppm vs. 100–200 ppm, respectively) (Cortecci et al., 2005; Fernandez-Turiel et al., 2005). Low Mg concentrations also likely limit the precipitation of authigenic Mg-silicates (e.g., sepiolite), although further studies at El Tatio are required for conclusive evidence (Jones et al.,

2003; Leguey et al., 2010). In contrast to Mg-driven cation-bridging, silica precipitation in floating El Tatio mats is driven by evaporation, forming opaque crusts which inhibit photosynthetic activity. The results from both studies indicate that microbial silicification is a result of complex relationships between silica chemistry, microbial metabolisms, and environmental processes.

## 6 | CONCLUSIONS

This study elaborates on previous models of silica precipitation in hydrothermal microbial communities by combining chemical, environmental, genetic, and microscopic datasets from two streams in El Tatio, Chile. Floating microbial mats in Vicuna Stream reach silica saturation in two temporally separate stages: daytime evaporation and nighttime cooling. Based on crust distribution on subaerially exposed mats, evaporation is more likely to influence the spatial patterns of silica crusts than nighttime cooling. While nighttime conditions are less likely to govern the spatial patterns of crust formation, cooler temperatures coupled with lower pH in the absence of photosynthesis still maintain relatively favorable conditions to sustain silica crusts until the next evaporative cycle.

With repeated diurnal cycles of daytime evaporation and nighttime cooling, Vicuna Stream crusts become ~1–2 mm thick, enough to attenuate more than 90% of PAR. At temperatures above 30–40°C, such light attenuation begins to inhibit oxygenic photosynthesis, decreasing both  $\text{O}_2$  concentrations and pH underneath crusts. Lower pH values below crusts produce more highly silica-saturated conditions than adjacent unencrusted mats, decreasing the potential for the dissolution of silica crusts. In essence, a modest feedback loop is formed once crusts reach critical thicknesses beyond 1 mm, creating light-limited, less alkaline mats, which are more likely to foster the precipitation and growth of silica crusts.

Silica precipitation is rapid enough to preserve cells of various microbial morphologies, including relatively large filamentous cells, most likely representing cyanobacteria. Filaments within different layers of silica crust exhibit different qualities of preservation, indicating multiple generations of crust precipitation. However, no significant growth or diminishment of crust surface areas was observed over one week of observation and no fully silicified microbialites were preserved around either location of study. While evaporative wicking drives silica precipitation on floating mats, undersaturated stream waters with  $\text{SiO}_2$  concentrations below 150 ppm prohibit the progression of fragile crusts into consolidated sinters and do not favor subaqueous sinter formation. Instead, prolonged exposure fosters crust fragmentation rather than sinter formation. This study concludes that 1) evaporative silicification can occur and preserve microbial cells in relatively low-silica environments, and 2) extensive silicification can diminish oxygenic photosynthesis via light attenuation in microbial mats above 30–40°C, but 3) evaporative wicking is unlikely to produce well-cemented sinters in solutions below 200 ppm  $\text{SiO}_2$ .

## ACKNOWLEDGMENTS

This research is supported by a European Research Council Consolidator Grant #646894 (to MAVZ). The authors would like to thank the staff of the El Tatio Geyser Field for permission to sample in the area. KOK was supported by the Natural Science and Engineering Research Council of Canada. This is IGP contribution nr. 4247.

[Correction added on 02 November 2021, after first online publication: The Acknowledgments section has been updated in this revised version of the article.]

## CONFLICT OF INTEREST

The authors have no conflict of interest to report.

## ORCID

Dylan T. Wilmeth  <https://orcid.org/0000-0002-6299-6267>

## REFERENCES

- Alexander, G. B., Heston, W. M., & Iler, R. K. (1954). The solubility of amorphous silica in water. *The Journal of Physical Chemistry*, 58, 453–455. <https://doi.org/10.1021/j150516a002>.
- Al-Najjar, M. A. A., de Beer, D., Kühl, M., & Polerecky, L. (2012). Light utilization efficiency in photosynthetic microbial mats: Fate of light energy in photosynthetic microbial mats. *Environmental Microbiology*, 14, 982–992. <https://doi.org/10.1111/j.1462-2920.2011.02676.x>.
- Benning, L. G., Phoenix, V. R., Yee, N., & Konhauser, K. O. (2004). The dynamics of cyanobacterial silicification: an infrared micro-spectroscopic investigation. *Geochimica Et Cosmochimica Acta*, 68, 743–757. [https://doi.org/10.1016/S0016-7037\(03\)00488-5](https://doi.org/10.1016/S0016-7037(03)00488-5).
- Berelson, W. M., Corsetti, F. A., Pepe-Ranney, C., Hammond, D. E., Beaumont, W., & Spear, J. R. (2011). Hot spring siliceous stromatolites from Yellowstone National Park: assessing growth rate and laminae formation: Siliceous stromatolite growth rates. *Geobiology*, 9, 411–424. <https://doi.org/10.1111/j.1472-4669.2011.00288.x>.
- Cady, S. L., & Farmer, J. D. (1996). Fossilization Processes in Siliceous Thermal Springs: Trends in Preservation Along Thermal Gradients. In G. R. Bock, & J. A. Goode (Eds.), *Evolution of hydrothermal ecosystems on Earth (and Mars?)* (pp. 150–173). John Wiley & Sons Ltd.
- Campbell, K. A., Lynne, B. Y., Handley, K. M., Jordan, S., Farmer, J. D., Guido, D. M., Foucher, F., Turner, S., & Perry, R. S. (2015). Tracing biosignature preservation of geothermally silicified microbial textures into the geological record. *Astrobiology*, 15, 858–882. <https://doi.org/10.1089/ast.2015.1307>.
- Campbell, K. A., Rodgers, K. A., Brotheridge, J. M. A., & Browne, P. R. L. (2002). An unusual modern silica-carbonate sinter from Pavlova spring, Ngatamariki, New Zealand. *Sedimentology*, 49, 835–854. <https://doi.org/10.1046/j.1365-3091.2002.00473.x>.
- Caporaso, J. G., Kuczynski, J., Stombaugh, J., Bittinger, K., Bushman, F. D., Costello, E. K., Fierer, N., Peña, A. G., Goodrich, J. K., Gordon, J. I., Huttley, G. A., Kelley, S. T., Knights, D., Koenig, J. E., Ley, R. E., Lozupone, C. A., McDonald, D., Muegge, B. D., Pirrung, M., ... Knight, R. (2010). QIIME allows analysis of high-throughput community sequencing data. *Nature Methods*, 7, 335–336. <https://doi.org/10.1038/nmeth.f.303>.
- Castenholz, R. W. (1973). Ecology of blue-green algae in hot springs. In N. G. Carrand, & B. A. Whitton (Eds.), *The Biology of Blue-Green Algae* (pp. 379–414). Blackwell Scientific Publications.
- Cockell, C. (2000). The ultraviolet environment of mars: biological implications past, present, and future. *Icarus*, 146, 343–359. <https://doi.org/10.1006/icar.2000.6393>.
- Cnossen I., Sanz-Forcada J., Favata F., Witasse O., Zegers T., Arnold N. F. (2007). Habitat of early life: Solar X-ray and UV radiation at Earth's surface 4–3.5 billion years ago. *Journal of Geophysical Research*, 112, (E2), <http://dx.doi.org/10.1029/2006je002784>
- Cortecchi, G., Boschetti, T., Mussi, M., Lameli, C. H., Mucchino, C., & Barbieri, M. (2005). New chemical and original isotopic data on waters from El Tatio geothermal field, northern Chile. *Geochemical Journal*, 39, 547–571. <https://doi.org/10.2343/geochemj.39.547>.
- DeSantis, T. Z., Hugenholtz, P., Larsen, N., Rojas, M., Brodie, E. L., Keller, K., Huber, T., Dalevi, D., Hu, P., & Andersen, G. L. (2006). Greengenes, a Chimera-Checked 16S rRNA Gene Database and Workbench Compatible with ARB. *Applied and Environmental Microbiology*, 72, 5069–5072. <https://doi.org/10.1128/AEM.03006-05>.
- DGA (2017). Direccion general de aguas de chile, Información Oficial Hidrometeorológica y de Calidad de Aguas en Línea. <https://dga.mop.gob.cl/> (Accessed March 2017).
- Djokic, T., Van Kranendonk, M. J., Campbell, K. A., Walter, M. R., & Ward, C. R. (2017). Earliest signs of life on land preserved in ca. 3.5 Ga hot spring deposits. *Nature Communications Nature Communications*, 8, 15263. <https://doi.org/10.1038/ncomms15263>.
- Dowd, S. E., Sun, Y., Wolcott, R. D., Domingo, A., & Carroll, J. A. (2008). Bacterial tag-encoded FLX Amplicon Pyrosequencing (bTEFAP) for microbiome studies: bacterial diversity in the ileum of newly weaned salmonella -infected pigs. *Foodborne Pathogens and Disease*, 5, 459–472.
- Dupraz, C., Reid, R. P., Braissant, O., Decho, A. W., Norman, R. S., & Visscher, P. T. (2009). Processes of carbonate precipitation in modern microbial mats. *Earth-Science Reviews*, 96, 141–162. <https://doi.org/10.1016/j.earscirev.2008.10.005>.
- Engel, A. S., Johnson, L. R., & Porter, M. L. (2013). Arsenite oxidase gene diversity among *Chloroflexi* and *Proteobacteria* from El Tatio Geyser Field, Chile. *FEMS Microbiology Ecology*, 83, 745–756.
- Epping, E., & Kuhl, M. (2000). The responses of photosynthesis and oxygen consumption to short-term changes in temperature and irradiance in a cyanobacterial mat (Ebro Delta, Spain). *Environmental Microbiology*, 2, 465–474. <https://doi.org/10.1046/j.1462-2920.2000.00129.x>.
- Fernandez-Turiel, J. L., Garcia-Valles, M., Gimeno-Torrente, D., Saavedra-Alonso, J., & Martinez-Manent, S. (2005). The hot spring and geyser sinters of El Tatio, Northern Chile. *Sedimentary Geology*, 180, 125–147. <https://doi.org/10.1016/j.sedgeo.2005.07.005>.
- Fouke, B. W. (2011). Hot-spring Systems Geobiology: abiotic and biotic influences on travertine formation at Mammoth Hot Springs, Yellowstone National Park, USA: Hot-spring systems geobiology. *Sedimentology*, 58, 170–219. <https://doi.org/10.1111/j.1365-3091.2010.01209.x>.
- Fouke, B. W., Farmer, J. D., Des Marais, D. J., Pratt, L., Sturchio, N. C., Burns, P. C., & Discipulo, M. K. (2000). Depositional facies and aqueous-solid geochemistry of travertine-depositing hot springs (Angel Terrace, Mammoth Hot Springs, Yellowstone National Park, U.S.A.). *Journal of Sedimentary Research*, 70, 565–585. <https://doi.org/10.1306/2DC40929-0E47-11D7-8643000102C1865D>.
- Fournier, R. O. (1985). The behaviour of silica in hydrothermal solutions. In: B. R. Berger, & P. M. Bethke (eds.) *Geology and Geochemistry of Epithermal Systems. Reviews in Economic Geology*, Vol. 2. The Economic Geology Publishing Co., 45–61.
- Glendon, J. A., & Pfaff, R. M. (2003). *The Extraordinary Thermal Activity of El Tatio Geyser Field, Antofagasta Region, Chile*. 8. GOSA Trans, pp. 31–78.
- Gong, J., Munoz-Saez, C., Wilmeth, D. T., Myers, K. D., Homann, M., Arp, G., & Skok, J. R. van Zuilen, M. A. (in review) Morphogenesis of digitate structures in hot spring silica sinters of the El Tatio geothermal field, Chile. *Geobiology*.
- Gong, J., Myers, K. D., Munoz-Saez, C., Homann, M., Rouillard, J., Wirth, R., Schreiber, A., & van Zuilen, M. A. (2020a). Formation and Preservation of Microbial Palisade Fabric in Silica Deposits from

- El Tatio, Chile. *Astrobiology*, 20, 500–524. <https://doi.org/10.1089/ast.2019.2025>.
- Guidry, S. A., & Chafetz, H. S. (2002). Factors governing subaqueous siliceous sinter precipitation in hot springs: examples from Yellowstone National Park, USA. *Sedimentology*, 49, 1253–1267. <https://doi.org/10.1046/j.1365-3091.2002.00494.x>.
- Gunnarsson, I., & Arnórsson, S. (2000). Amorphous silica solubility and the thermodynamic properties of H<sub>4</sub>SiO<sub>4</sub> in the range of 0° to 350°C at Psat. *Geochimica Et Cosmochimica Acta*, 64, 2295–2307. [https://doi.org/10.1016/S0016-7037\(99\)00426-3](https://doi.org/10.1016/S0016-7037(99)00426-3).
- Handley, K. M., Campbell, K. A., Mountain, B. W., & Browne, P. R. L. (2005). Abiotic-biotic controls on the origin and development of spicular sinter: in situ growth experiments, Champagne Pool, Waiotapu, New Zealand. *Geobiology*, 3, 93–114. <https://doi.org/10.1111/j.1472-4669.2005.00046.x>.
- Handley Kim M., Turner Sue J., Campbell Kathleen A., Mountain Bruce W. (2008). Silicifying Biofilm Exopolymers on a Hot-Spring Microstromatolite: Templating Nanometer-Thick Laminae. *Astrobiology*, 8, (4), 747–770. <http://dx.doi.org/10.1089/ast.2007.0172>
- Havig J. R., Hamilton T. L. (2019). Hypolithic Photosynthesis in Hydrothermal Areas and Implications for Cryptic Oxygen Oases on Archean Continental Surfaces. *Frontiers in Earth Science*, 7, <http://dx.doi.org/10.3389/feart.2019.00015>
- Hinman, N. W., & Lindstrom, R. F. (1996). Seasonal changes in silica deposition in hot spring systems. *Chemical Geology*, 132, 237–246. [https://doi.org/10.1016/S0009-2541\(96\)00060-5](https://doi.org/10.1016/S0009-2541(96)00060-5).
- Jones, B., Konhauser, K. O., Renaut, R., & Wheeler, R. (2004). Microbe silicification in Iodine Pool, Waimangu geothermal area, North Island, New Zealand: Implications for recognition and identification of ancient silicified microbes. *Journal of the Geological Society of London*, 161, 983–993.
- Jones, B., & Renaut, R. W. (1997). Formation of silica oncoids around geysers and hot springs at El Tatio, northern Chile. *Sedimentology*, 44, 287–304. <https://doi.org/10.1111/j.1365-3091.1997.tb01525.x>.
- Jones, B., Renaut, R. W., & Konhauser, K. O. (2005). Genesis of large siliceous stromatolites at Frying Pan Lake, Waimangu geothermal field, North Island, New Zealand. *Sedimentology*, 52, 1229–1252. <https://doi.org/10.1111/j.1365-3091.2005.00739.x>.
- Jones, B., Renaut, R. W., & Rosen, M. R. (1998). Microbial biofacies in hot-spring sinters; a model based on Ohaaki Pool, North Island, New Zealand. *Journal of Sedimentary Research*, 68, 413–434. <https://doi.org/10.2110/jsr.68.413>.
- Jones, B., Renaut, R. W., & Rosen, M. R. (2003). Silicified microbes in a geyser mound: the enigma of low-temperature cyanobacteria in a high-temperature setting. *Palaios*, 18, 87–109. [https://doi.org/10.1669/0883-1351\(2003\)18<87:SMIAGM>2.0.CO;2](https://doi.org/10.1669/0883-1351(2003)18<87:SMIAGM>2.0.CO;2).
- Jorgensen, B. B., Revsbech, N. P., & Cohen, Y. (1983). Photosynthesis and structure of benthic microbial mats: Microelectrode and SEM studies of four cyanobacterial communities: Photosynthesis of cyanobacterial mats. *Limnology and Oceanography*, 28, 1075–1093. <https://doi.org/10.4319/lo.1983.28.6.1075>.
- Konhauser, K. O., & Ferris, F. G. (1996). Diversity of iron and silica precipitation by microbial mats in hydrothermal waters, Iceland: Implications for Precambrian iron formations. *Geology*, 24(4), 323.
- Konhauser, K. O., Jones, B., Phoenix, V. R., Ferris, G., & Renaut, R. W. (2004). The microbial role in hot spring silicification. *Ambio*, 33, 552–558. <https://doi.org/10.1579/0044-7447-33.8.552>.
- Konhauser, K. O., Jones, B., Reysenbach, A.-L., & Renaut, R. W. (2003). Hot spring sinters: keys to understanding Earth's earliest life forms. *Canadian Journal of Earth Sciences*, 40, 1713–1724. <https://doi.org/10.1139/e03-059>.
- Konhauser, K. O., Phoenix, V. R., Bottrell, S. H., Adams, D. G., & Head, I. M. (2001). Microbial-silica interactions in Icelandic hot spring sinter: possible analogues for some Precambrian siliceous stromatolites. *Sedimentology*, 48, 415–433. <https://doi.org/10.1046/j.1365-3091.2001.00372.x>.
- Kuhl, M., Glud, R. N., Ploug, H., & Ramsing, N. B. (1996). Microenvironmental control of photosynthesis and photosynthesis-coupled respiration in an epilithic cyanobacterial biofilm. *Journal of Phycology*, 32, 799–812.
- Lalonde, S. V., Konhauser, K. O., Reysenbach, A.-L., & Ferris, F. G. (2005). The experimental silicification of Aquificales and their role in hot spring sinter formation. *Geobiology*, 3, 41–52. <https://doi.org/10.1111/j.1472-4669.2005.00042.x>.
- Leguey, S., De León, D. R., Ruiz, A. I., & Cuevas, J. (2010). The role of biomineralization in the origin of sepiolite and dolomite. *American Journal of Science*, 310, 165–193. <https://doi.org/10.2475/03.2010.02>.
- Leo, R. F., & Barghoorn, E. S. (1976). Silicification of wood. *Botanical Museum Leaflets, Harvard University*, 25, 1–47. <https://doi.org/10.5962/p.295209>.
- Lichtenberg, M., Brodersen, K. E., & Kühl, M. (2017). Radiative energy budgets of phototrophic surface-associated microbial communities and their photosynthetic efficiency under diffuse and collimated light. *Frontiers in Microbiology*, 8.
- Lynne, B. Y., Boudreau, A., Smith, I. J., & Smith, G. J. (2019). Silica accumulation rates for siliceous sinter at Orakei Korako geothermal field, Taupo Volcanic Zone, New Zealand. *Geothermics*, 78, 50–61. <https://doi.org/10.1016/j.geothermics.2018.11.007>.
- Manning-Berg, A. R., & Kah, L. C. (2017). Proterozoic microbial mats and their constraints on environments of silicification. *Geobiology*, 15, 469–483.
- Moore, K. R., Gong, J., Pajusalu, M., Skoog, E. J., Xu, M., Feliz Soto, T., Sojo, V., Matreux, T., Baldes, M. J., Braun, D., & Williford, K. (2021). A new model for silicification of cyanobacteria in Proterozoic tidal flats. *Geobiology*, 19(5), 438–449.
- Moore, K. R., Pajusalu, M., Gong, J., Sojo, V., Matreux, T., Braun, D., & Bosak, T. (2020). Biologically mediated silicification of marine cyanobacteria and implications for the Proterozoic fossil record. *Geology*, 48, 862–866. <https://doi.org/10.1130/G47394.1>.
- Mountain, B. W., Benning, L. G., & Boerema, J. A. (2003). Experimental studies on New Zealand hot spring sinters: rates of growth and textural development. *Canadian Journal of Earth Sciences*, 40(11), 1643–1667. <https://doi.org/10.1139/e03-068>.
- Munoz-Saez, C., Manga, M., & Hurwitz, S. (2018). Hydrothermal discharge from the El Tatio basin, Atacama, Chile. *Journal of Volcanology and Geothermal Research*, 361, 25–35. <https://doi.org/10.1016/j.jvolgeores.2018.07.007>.
- Munoz-Saez, C., Manga, M., Hurwitz, S., Rudolph, M. L., Namiki, A., & Wang, C.-Y. (2015). Dynamics within geyser conduits, and sensitivity to environmental perturbations: Insights from a periodic geyser in the El Tatio geyser field, Atacama Desert, Chile. *Journal of Volcanology and Geothermal Research*, 292, 41–55. <https://doi.org/10.1016/j.jvolgeores.2015.01.002>.
- Munoz-Saez C., Saltiel S., Manga M., Nguyen C., Gonnermann H. (2016). Physical and hydraulic properties of modern sinter deposits: El Tatio, Atacama. *Journal of Volcanology and Geothermal Research*, 325, 156–168. <http://dx.doi.org/10.1016/j.jvolgeores.2016.06.026>
- Nicolau, C., Reich, M., & Lynne, B. (2014). Physico-chemical and environmental controls on siliceous sinter formation at the high-altitude El Tatio geothermal field, Chile. *Journal of Volcanology and Geothermal Research*, 282, 60–76. <https://doi.org/10.1016/j.jvolgeores.2014.06.012>.
- Orange, F., Lalonde, S. V., & Konhauser, K. O. (2013). The formation and preservation of *Synechococcus elongatus* cell moulds in simulated silica sinter: Implications for the identification of microfossils. *Geomicrobiology Journal*, 30, 327–336.
- Orange, F., Lalonde, S. V., & Konhauser, K. O. (2018). Experimental simulation of evaporation-driven silica sinter formation and microbial silicification in hot spring systems. *Astrobiology*, 13, 163–176. <https://doi.org/10.1089/ast.2012.0887>.

- Parenteau, M. N., & Cady, S. L. (2010). Microbial biosignatures in iron-mineralized phototrophic mats at Chocolate Pots Hot Springs, Yellowstone National Park, United States. *Palaio*, 25, 97–111. <https://doi.org/10.2110/palo.2008.p08-133r>.
- Phoenix, V. R., Bennett, P. C., Engel, A. S., Tyler, S. W., & Ferris, F. G. (2006). Chilean high-altitude hot-spring sinters: a model system for UV screening mechanisms by early Precambrian cyanobacteria. *Geobiology*, 4, 15–28. <https://doi.org/10.1111/j.1472-4669.2006.00063.x>.
- Phoenix, V. R., & Konhauser, K. O. (2008). Benefits of bacterial biomineralization. *Geobiology*, 6, 303–308. <https://doi.org/10.1111/j.1472-4669.2008.00147.x>.
- Phoenix, V. R., Konhauser, K. O., Adams, D. G., & Bottrell, S. H. (2001). Role of biomineralization as an ultraviolet shield: Implications for Archean life. *Geology*, 29, 823–826. [https://doi.org/10.1130/0091-7613\(2001\)029<0823:ROBAAU>2.0.CO;2](https://doi.org/10.1130/0091-7613(2001)029<0823:ROBAAU>2.0.CO;2).
- Phoenix, V. R., Konhauser, K. O., & Ferris, F. G. (2003). Experimental study of iron and silica immobilization by bacteria in mixed Fe-Si systems: implications for microbial silicification in hot springs. *Canadian Journal of Earth Sciences*, 40, 1669–1678. <https://doi.org/10.1139/e03-044>.
- Phoenix, V. R., Martinez, R. E., Konhauser, K. O., & Ferris, F. G. (2002). Characterization and Implications of the Cell Surface Reactivity of *Calothrix* sp. Strain KC97. *Applied and Environmental Microbiology*, 68, 4827–4834.
- Plenge, M. F., Engel, A. S., Omelon, C. R., & Bennett, P. C. (2017). Thermophilic archaeal diversity and methanogenesis from El Tatio Geyser Field, Chile. *Geomicrobiology Journal*, 34, 220–230. <https://doi.org/10.1080/01490451.2016.1168496>.
- Pringault, O., de Wit, R., & Camoin, G. (2005). Irradiance regulation of photosynthesis and respiration in modern marine microbialites built by benthic cyanobacteria in a Tropical Lagoon (New Caledonia). *Microbial Ecology*, 49, 604–616. <https://doi.org/10.1007/s00248-004-0102-y>.
- Revsbech, N. P., Jorgensen, B. B., Blackburn, T. H., & Cohen, Y. (1983). Microelectrode studies of the photosynthesis and O<sub>2</sub>, H<sub>2</sub>S, and pH profiles of a microbial mat1: O<sub>2</sub>, H<sub>2</sub>S, and pH in microbial mat. *Limnology and Oceanography*, 28, 1062–1074.
- Ruff, S. W., Campbell, K. A., Van Kranendonk, M. J., Rice, M. S., & Farmer, J. D. (2020). The case for ancient hot springs in Gusev Crater, Mars. *Astrobiology*, 20, 475–499. <https://doi.org/10.1089/ast.2019.2044>.
- Ruff, S. W., & Farmer, J. D. (2016). Silica deposits on Mars with features resembling hot spring biosignatures at El Tatio in Chile. *Nature Communications*, 7, 13554. <https://doi.org/10.1038/ncomm513554>.
- Schultze-Lam, S., Ferris, F. G., Konhauser, K. O., & Wiese, R. G. (1995). In situ silicification of an Icelandic hot spring microbial mat: implications for microfossil formation. *Canadian Journal of Earth Sciences*, 32, 2021–2026. <https://doi.org/10.1139/e95-155>.
- Slagter, S., Reich, M., Munoz-Saez, C., Southon, J., Morata, D., Barra, F., Gong, J., & Skok, J. R. (2019). Environmental controls on silica sinter formation revealed by radiocarbon dating. *Geology*, 47, 330–334. <https://doi.org/10.1130/G45859.1>.
- Smith, R.M., Martell, A.E. & Motekaitis, R.J. (2004). NIST Standard Reference Database, 46.
- Som, S. M., Buick, R., Hagadorn, J. W., Blake, T. S., Perreault, J. M., Harnmeijer, J. P., & Catling, D. C. (2016). Earth's air pressure 2.7 billion years ago constrained to less than half of modern levels. *Nature Geoscience*, 9, 448–451. <https://doi.org/10.1038/ngeo2713>.
- Som, S. M., Catling, D. C., Harnmeijer, J. P., Polivka, P. M., & Buick, R. (2012). Air density 2.7 billion years ago limited to less than twice modern levels by fossil raindrop imprints. *Nature*, 484, 359–362. <https://doi.org/10.1038/nature10890>.
- Tassi F., Martinez C., Vaselli O., Capaccioni B., Viramonte J. (2005). Light hydrocarbons as redox and temperature indicators in the geothermal field of El Tatio (northern Chile). *Applied Geochemistry*, 20, (11), 2049. –2062. <http://dx.doi.org/10.1016/j.apgeochem.2005.07.013>
- Trewin N. H., Fayers S. R., Kelman R. (2003). Subaqueous silicification of the contents of small ponds in an Early Devonian hot-spring complex, Rhynie, Scotland. *Canadian Journal of Earth Sciences*, 40, (11), 1697. –1712. <http://dx.doi.org/10.1139/e03-065>
- Trujillo, P. (1969). *Estudio para el desarrollo geotérmico en el norte de Chile- Manifestaciones termales de El Tatio*. CORFO Project Report, Provincia de Antofagasta.
- Walter, M. R. (1976) Chapter 8.8 Hot-Spring Sediments in Yellowstone National Park. In: *Developments in Sedimentology*. Elsevier, pp. 489–498.
- Walter, M. R., Desmarais, D., Farmer, J. D., & Hinman, N. W. (1996). Lithofacies and Biofacies of Mid-Paleozoic Thermal Spring Deposits in the Drummond Basin, Queensland, Australia. *PALAIOS*, 11, 497. <https://doi.org/10.2307/3515187>.
- Walters, W., Hyde, E. R., Berg-Lyons, D., Ackermann, G., Humphrey, G., Parada, A., Gilbert, J. A., Jansson, J. K., Caporaso, J. G., Fuhrman, J. A., Apprill, A., & Knight, R. (2016). Improved bacterial 16S rRNA Gene (V4 and V4-5) and fungal internal transcribed spacer marker gene primers for microbial community surveys. *mSystems*, 1(1), e00009–15. <https://doi.org/10.1128/mSystems.00009-15>.
- Weiner, S., & Dove, P.M. (2003). An overview of biomineralization processes and the problem of the vital effect. *Reviews in Mineralogy and Geochemistry*, 54, 1–29. <https://doi.org/10.2113/0540001>.
- Wieland, A., & Kühl, M. (2000). Irradiance and temperature regulation of oxygenic photosynthesis and O<sub>2</sub> consumption in a hypersaline cyanobacterial mat (Solar Lake, Egypt). *Marine Biology*, 137, 71–85. <https://doi.org/10.1007/s002270000331>.
- Wilmeth, D. T., Corsetti, F. A., Beukes, N. J., Awramik, S. M., Petryshyn, V., Spear, J. R., & Celestian, A. J. (2019). Neoproterozoic (2.7 Ga) lacustrine stromatolite deposits in the Hartbeesfontein Basin, Ventersdorp Supergroup, South Africa: Implications for oxygen oases. *Precambrian Research*, 320, 291–302.
- Wilmeth, D. T., Johnson, H. A., Stamps, B. W., Berelson, W. M., Stevenson, B. S., Nunn, H. S., Grim, S. L., Dillon, M. L., Paradis, O., Corsetti, F. A., & Spear, J. R. (2018). Environmental and biological influences on carbonate precipitation within hot spring microbial mats in little hot creek CA. *Frontiers in Microbiology*, 9, 1464. <https://doi.org/10.3389/fmicb.2018.01464>.
- Yee, N., Phoenix, V. R., Konhauser, K. O., Benning, L. G., & Ferris, F. G. (2003). The effect of cyanobacteria on silica precipitation at neutral pH: implications for bacterial silicification in geothermal hot springs. *Chemical Geology*, 199, 83–90. [https://doi.org/10.1016/S0009-2541\(03\)00120-7](https://doi.org/10.1016/S0009-2541(03)00120-7).
- Zeil, W. (1959). Junger Vulkanismus in der Hochkordillere der Provinz Antofagasta (Chile). *Geologische Rundschau*, 48, 218–232. <https://doi.org/10.1007/BF01801827>.

## SUPPORTING INFORMATION

Additional supporting information may be found in the online version of the article at the publisher's website.

**How to cite this article:** Wilmeth, D. T., Myers, K. D., Lalonde, S. V., Mänd, K., Konhauser, K. O., Grandin, P., & van Zuilen, M. A. (2022). Evaporative silicification in floating microbial mats: patterns of oxygen production and preservation potential in silica-undersaturated streams, El Tatio, Chile. *Geobiology*, 20, 310–330. <https://doi.org/10.1111/gbi.12476>